minerals

MDPI

Article

Mineralization Age and Hydrothermal Evolution of the Fukeshan Cu (Mo) Deposit in the Northern Great Xing'an Range, Northeast China: Evidence from Fluid Inclusions, H–O–S–Pb Isotopes, and Re–Os Geochronology

Yong-gang Sun [1,2,*], Bi-le Li [1,*], Qing-feng Ding [1], Yuan Qu [3], Cheng-ku Wang [3], Lin-lin Wang [1,4] and Qing-lin Xu [5]

[1] College of Earth Sciences, Jilin University, Changchun 130061, China; dingqf@jlu.edu.cn (Q.-f.D.); wanglinlin@jlu.edu.cn (L.-l.W.)
[2] Geological Survey Institute of Jilin Province, Changchun 130102, China
[3] Geological Science Institute of Heilongjiang Province, Harbin 150088, China; xianglanliangku@163.com (Y.Q.); ck13351908711@163.com (C.-k.W.)
[4] Key Laboratory of Mineral Resources Evaluation in Northeast Asia, Ministry of Land and Resources, Changchun 130061, China
[5] College of Earth Science and Engineering, Shandong University of Science and Technology, Qingdao 266590, China; xql_618@163.com
* Correspondence: sunyg18@mails.jlu.edu.cn (Y.-g.S.); libl@jlu.edu.cn (B.-l.L.)

Received: 15 June 2020; Accepted: 29 June 2020; Published: 30 June 2020

Abstract: The Fukeshan Cu (Mo) deposit is a newfound porphyry deposit in the northern Great Xing'an Range (GXR), northeast China. In this paper, we present results of chalcopyrite Re–Os geochronology, microthermometry of the fluid inclusions (FIs), and isotopic (H–O–S–Pb) compositions of the Fukeshan Cu (Mo) deposit. Its ore-forming process can be divided into sulfide-barren quartz veins (A vein; stage I), quartz + chalcopyrite + pyrite veins (B vein; stage II), quartz + polymetallic sulfide veins (D vein; stage III), and barren quartz + carbonate ± pyrite veins (E vein; stage IV), with Cu mineralization mainly occurred in stage II. Three types of FIs are identified in this deposit: liquid-rich two-phase (L-type) FIs, vapor-rich two-phase (V-type) FIs, daughter mineral-bearing three-phase (S-type) FIs. The homogenization temperatures of primary FIs hosted in quartz of stages I–IV are 381–494 °C, 282–398 °C, 233–340 °C, and 144–239 °C, with salinities of 7.2–58.6, 4.8–9.9, 1.4–7.9, and 0.9–3.9 wt. % NaCl equivalent, respectively. FIs microthermometry and H–O isotope data suggest that the ore-forming fluids were magmatic in origin and were gradually mixed with meteoric water from stages II to IV. Sulfur and lead isotope results indicate that the ore-forming materials of the Fukeshan Cu (Mo) deposit were likely to have originated from Late Jurassic intrusive rocks. The available data suggest that fluid cooling and incursions of meteoric water into the magmatic fluids were two important factors for Cu precipitation in the Fukeshan Cu (Mo) deposit. Chalcopyrite Re–Os dating yielded an isochron age of 144.7 ± 5.4 Ma, which is similar to the zircon U–Pb age of the quartz diorite porphyry, indicating that Late Jurassic quartz diorite porphyry and Cu mineralization occurred contemporaneously.

Keywords: Fukeshan Cu (Mo) deposit; fluid inclusions; H–O–S–Pb isotope; chalcopyrite Re–Os dating; Great Xing'an Range

1. Introduction

Being the largest Phanerozoic accretionary orogenic belt worldwide, the Central Asian Orogenic Belt (CAOB) documents the formation and evolution of Eurasia systematically [1–3], and is located between the Siberian Craton and the Tarim-North China Craton (Figure 1A) [4,5]. Northeast (NE) China located in the east of the CAOB (Figure 1A), and the Great Xing'an Range (GXR) situated in western NE China (Figure 1B), is an important polymetallic metallogenic belt in China [6,7], hosting a number of epithermal and orogenic Au deposits (e.g., Shabaosi Au deposit; Sandaowanzi Au deposit) [8,9], porphyry deposits (e.g., Duobaoshan Cu–Mo–(Au) deposit; Wunugetushan Cu–Mo deposit) [10,11], hydrothermal Ag–Pb–Zn deposits (e.g., Jiawula Pb–Zn–Ag deposit; Chaganbulagen Pb–Zn–Ag deposit) [12,13], and skarn Pb–Zn deposits (e.g., Baiyinnuo'er Zn–Pb deposit) [14–16]. In recent years, many Late Mesozoic porphyry deposits have been discovered in the northern GXR (Figure 1C), such as the Chalukou Mo (ca. 148 Ma) [17], the Daheishan Mo (ca. 147 Ma) [18], and the Xiaokele Cu (Mo) (ca. 150 Ma) deposits [19].

The newfound Fukeshan porphyry Cu (Mo) deposit is located in the northern GXR. Previous researches on the Fukeshan deposit were mainly concentrated on the geological characteristics [20,21], and the geochronology and geochemistry of intrusions [20,22]. These studies have reached a consensus that the Fukeshan Cu (Mo) deposit is a porphyry deposit. However, the source of the ore-forming materials, and the origin and evolution of the ore-forming fluids have not been constrained.

To address these issues, based on detailed core logging, this paper presents microthermometry of the fluid inclusions, isotopic (H–O–S–Pb) compositions, and chalcopyrite Re–Os geochronology. These results allowed us to further discuss the evolution of the ore-forming fluids and the possible metallogenic mechanism. This information can provide further prospecting direction of Late Mesozoic porphyry deposits in the northern GXR.

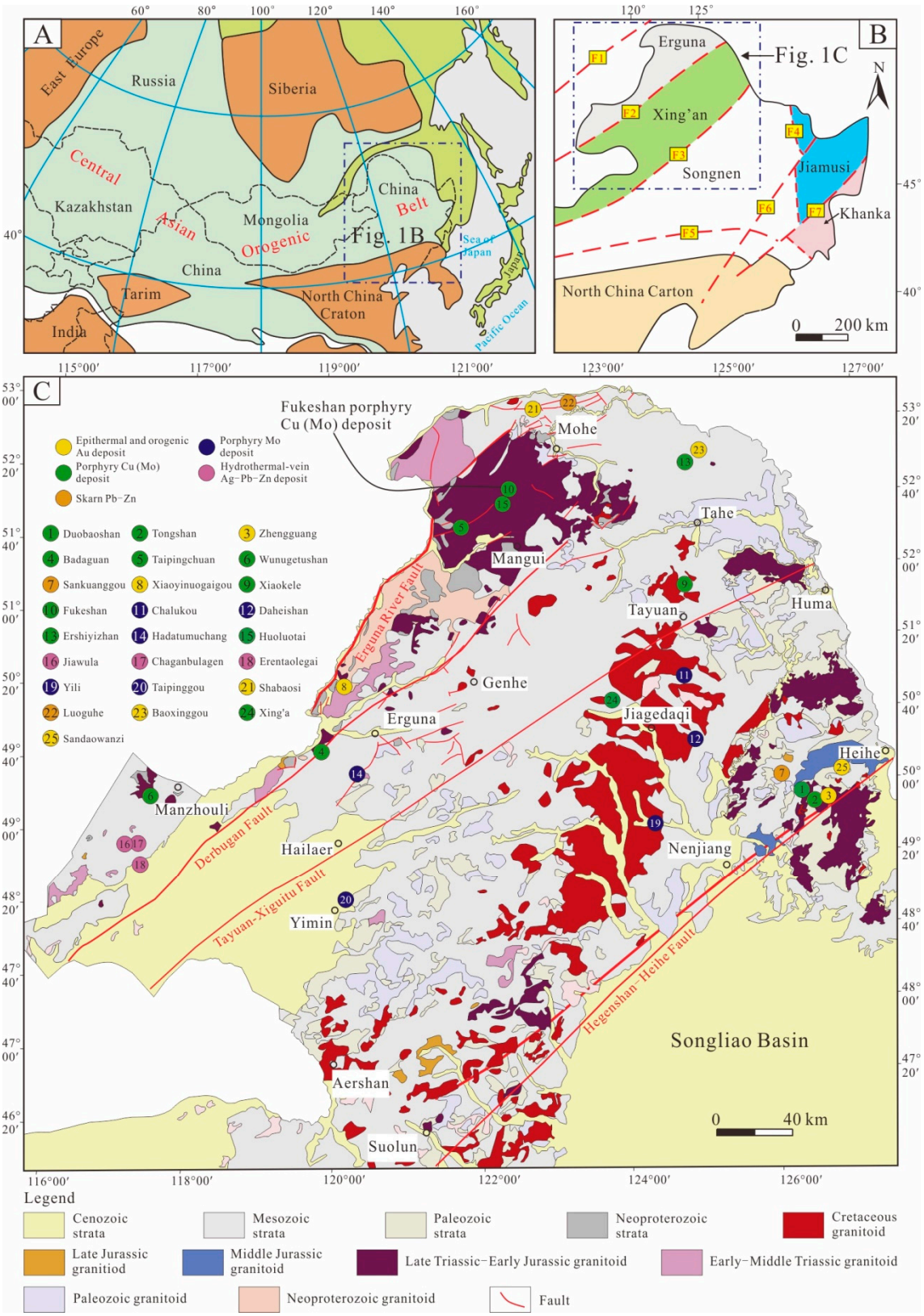

Figure 1. (**A**) Location of the Central Asian Orogenic Belt [1]. (**B**) Geological map of northeastern (NE) China [23]. Fault abbreviations: F1, Mongol–Okhotsk; F2, Tayuan–Xiguitu; F3, Hegenshan–Heihe; F4, Mudanjiang–Yilan; F5, Solonker–Xar Moron–Changchun–Yanji; F6, Jiamusi–Yilan; and F7, Dunhua–Mishan. (**C**) Geological map of the northern Great Xing'an Range (modified from [22]), showing the distribution of major ore deposits.

2. Regional Geology

NE China is segmented into the Khanka, Jiamusi, Songliao, Xing'an, and Erguna blocks from east to west, divided by the crustal-scale Dunhua–Mishan, Mudanjiang–Yilan, Hegenshan–Heihe, and Tayuan–Xiguitu faults (Figure 1B) [24]. Several micro-continental blocks collided and collaged successively with the continuous subduction of the Paleo-Asian Ocean during the Paleozoic [24,25]. After the Paleo-Asian Ocean closed, the Paleo-Pacific and the Mongol–Okhotsk tectonic region further superimposed and modified NE China during the Mesozoic [24,26].

The Fukeshan Cu (Mo) deposit is located in the northern part of the Erguna Block (Figure 1C). The Erguna Block is clamped between the Tayuan–Xiguitu and the Mongol–Okhotsk sutures (Figure 1B). The basement of the Erguna Block contains Precambrian metamorphic supracrustal rocks and scattered Paleoproterozoic and Neoproterozoic granitoids [27,28]. Outcropping strata mainly contain Paleozoic shallow marine sediments [29], widespread Mesozoic volcanic rocks, and minor terrigenous clastic rocks [30]. The major faults in the Erguna Block are the Late Mesozoic NE-trending Derbugan and Erguna River faults (Figure 1C) [27]. The intrusive rocks in the region are mainly Paleozoic and Mesozoic granites [24,31]. According to recent geochronological data, they can be divided into four stages: Early Paleozoic, Late Paleozoic, Late Triassic–Early Jurassic, and Late Jurassic–Early Cretaceous [24,26,32]. In addition, previous studies on Early Paleozoic post-orogenic granites in the Tahe–Mohe area and blueschist facies metamorphic rocks in Toudaoqiao have shown that the amalgamation of the Erguna and Xing'an blocks occurred at ca. 500 Ma along the Tayuan–Xiguitu suture zone (Figure 1C) [33,34].

3. Ore Deposit Geology

The Fukeshan Cu (Mo) deposit is located ~50 km southwest of the Mohe city, Heilongjiang Province (Figure 1C). NW-trending faults are developed in the deposit (Figure 2A). Multiphase intrusive rocks are observed in the Fukeshan mining area, including Early Jurassic medium-coarse-grained monzogranite (ca. 192 Ma), Late Jurassic medium-grained granodiorite (ca. 149 Ma) and quartz diorite porphyry (ca. 148 Ma), as well as Early Cretaceous intermediate and acidic dykes (Figure 2A,B) [22]. The quartz diorite porphyry intrudes the medium-coarse-grained monzogranite and medium-grained granodiorite rocks, Cu (Mo) mineralization is mainly developed in quartz diorite porphyry and its surrounding rock (Figure 2A,B), therefore the quartz diorite porphyry is considered to be the main host rock of the Cu (Mo) mineralization and closely related to hydrothermal alterations of the deposit. The quartz diorite porphyry is dark gray in color and has a massive structure with a porphyritic texture, it consists of 30–35% phenocrysts and 65–70% cryptocrystalline matrix, and phenocrysts are dominantly composed of plagioclase (20–25%), quartz (5–8%), and biotite (5–8%). A number of ore bodies have been found in the Fukeshan Cu (Mo) deposit, with Cu grades of 0.20–1.16% and Mo grades of 0.03–0.32% [22]. This deposit currently contains inferred ore reserves of >200,000 t, the reserves will increase with ongoing exploration.

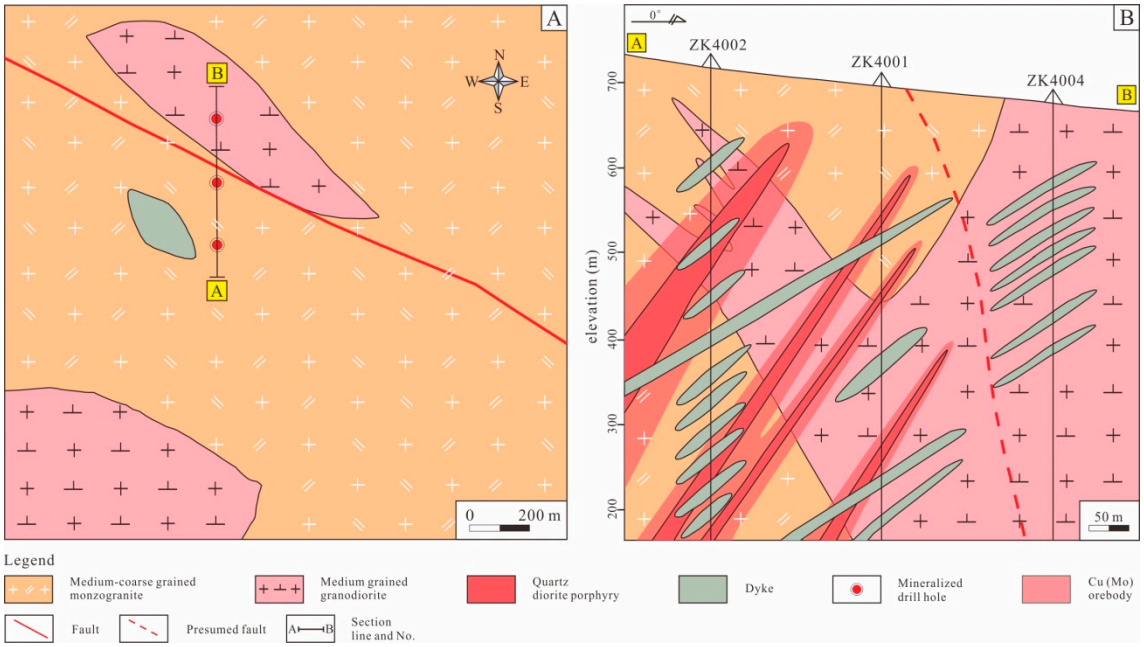

Figure 2. (**A**) Geological map of the Fukeshan Cu (Mo) deposit (modified from [21]). (**B**) Geological sections along the A–B exploration lines of the Fukeshan Cu (Mo) deposit (modified from [21]).

The mineralization and alteration characteristics of the Fukeshan Cu (Mo) deposit have been discussed based on the short wavelength infrared (SWIR) analysis [21], in this study, based on detailed field observations, mineral assemblages, and previous studies [21], alteration in the Fukeshan Cu (Mo) deposit can be divided, from early to late, into potassic, silicic, chlorite-illite/sericite, phyllic, and carbonate alterations. However, the alteration zonation is not obvious due to superposition of multiple post-metallogenic magmatism. Potassic and silicic alterations are mainly distributed in the quartz diorite porphyry and its surrounding rocks (Figure 3A–C). Potassic alteration are characterized by the mineral assemblage of secondary K-feldspar and biotite, irregular secondary K-feldspar was intensively developed in the quartz diorite porphyry, with fuzzy boundary between the crystals (Figure 3A). Metallic minerals that coexist with potassic and silicic alterations are mainly composed of magnetite, chalcopyrite, and minor molybdenite (Figures 3B and 4A–C). Chlorite-illite/sericite alteration contains chlorite, illite/sericite, and minor epidote, it only locally overprints the potassic and silicic alteration (Figure 3D,E). The main Cu mineralization is closely associated with potassic, silicic, and chlorite-illite/sericite alterations. Phyllic alteration is characterized by the mineral assemblage of quartz and sericite. Metallic minerals that coexist with phyllic alteration are mainly composed of pyrite, chalcopyrite, molybdenite, as well as minor sphalerite and galena. Phyllic alteration overprints the preexisting potassic, silicic, and chlorite-illite/sericite alterations. Sericite can completely/partially replace feldspars (Figure 3F). Minor veined and disseminated Cu (Mo) mineralization develop in the phyllic alteration zone.

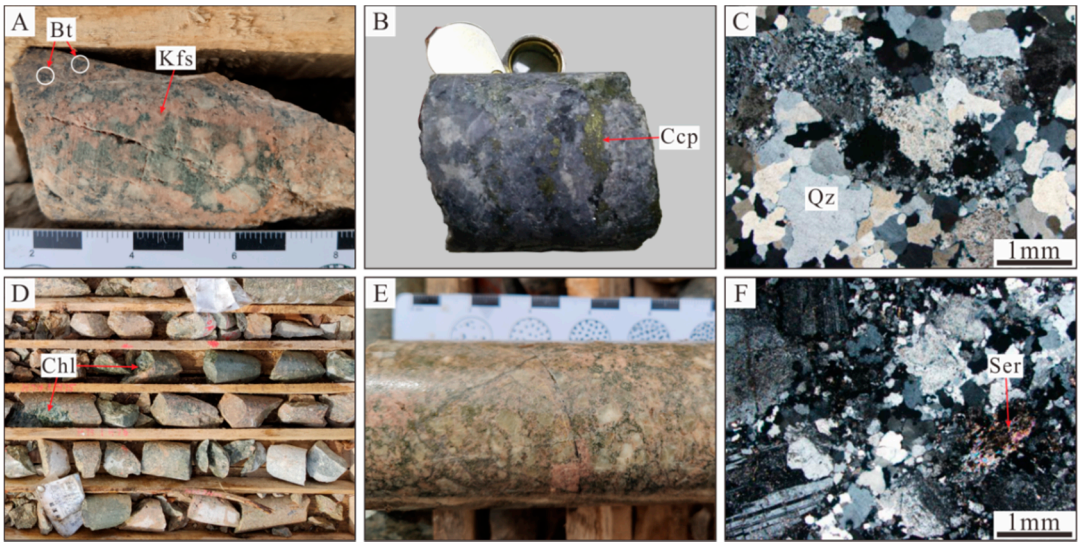

Figure 3. Photographs and photomicrographs of representative hydrothermal alteration features in the Fukeshan Cu (Mo) deposit. (**A**) Pervasive potassic alteration assemblages are mainly composed of secondary K-feldspar and biotite. (**B**) Intensive silicic alteration, associated with dense disseminated chalcopyrite. (**C**) Silicic alteration in the granodiorite. (**D**) Potassic alteration locally overprinted by chlorite alteration in the granodiorite. (**E**) Pervasive illite/sericite replaced feldspars and mafic minerals, showing a yellow-green color. (**F**) Phyllic alteration in the granodiorite, with sericite replace feldspar. Abbreviations: Qz, quartz; Kfs, K-feldspar; Bt, Biotite; Chl, Chlorite; Ser, sericite; and Ccp, chalcopyrite.

Based on mineral assemblages and crosscutting relationships between different veins in the Fukeshan Cu (Mo) deposit (Figure 4), we have identified four types of veins (i.e., A, B, D, and E veins) [35]. The vein sequence corresponds to four mineralization stages, from early to late: sulfide-barren quartz veins (A vein; stage I), quartz + chalcopyrite + pyrite veins (B vein; stage II), quartz + polymetallic sulfide veins (D vein; stage III), and barren quartz + carbonate ± pyrite veins (E vein; stage IV) (Figure 5). Their characteristics are described as follows.

Stage I is characterized by sulfide-barren quartz veins, similar to A veins as defined by [35], which generally consist of quartz (70–80 vol %), pyrite (5 vol %), chalcopyrite (ca. 5 vol %), magnetite (5–10 vol %), and hematite (ca. 5 vol %). Stage I veins are rarely observed. No obvious crosscutting relations are observed between stage I veins and other veins. These veins are discontinuous (Figure 4A) and are mostly concentrated in the potassic alteration core (relative to other late alterations), in which plagioclase and mafic minerals have been replaced pervasively by secondary K-feldspar and biotite, respectively. Stage II, which is the main Cu mineralization stage, is characterized by quartz + chalcopyrite + pyrite veins, similar to B veins described by [35]. Stage II veins are also mostly concentrated in the potassic alteration core relative to other late alterations. Stage II veins mainly contain quartz (65–75 vol %), chalcopyrite (5–10 vol %), pyrite (5–10 vol %), bornite (<5 vol %), and molybdenite (ca. 5 vol %). These veins are more continuous than stage I veins (Figure 4D). Stage III veins are generally associated with phyllic alteration, similar to D veins described by [35]. These veins are relatively continuous (Figure 4D,F), generally containing quartz (65–75 vol %), sericite (ca. 5 vol %), molybdenite (5–10 vol %), chalcopyrite (ca. 5 vol %), pyrite (ca. 5 vol %), sphalerite (<2 vol %), and galena (<2 vol %) (Figure 4E). Stage IV veins (E vein) generally contain quartz (>95 vol %), and minor carbonate and pyrite (Figure 4F,G). These veins postdating all early-formed veins and alteration types, represent the waning stage of the hydrothermal event in the Fukeshan Cu (Mo) deposit. Occasional pyrite (<3 vol %) is the only sulfide observed in stage IV veins. In addition, at shallow levels, the primary chalcopyrite was replaced by lower temperature supergene mineralization such as malachite and azurite (Figure 4H,I).

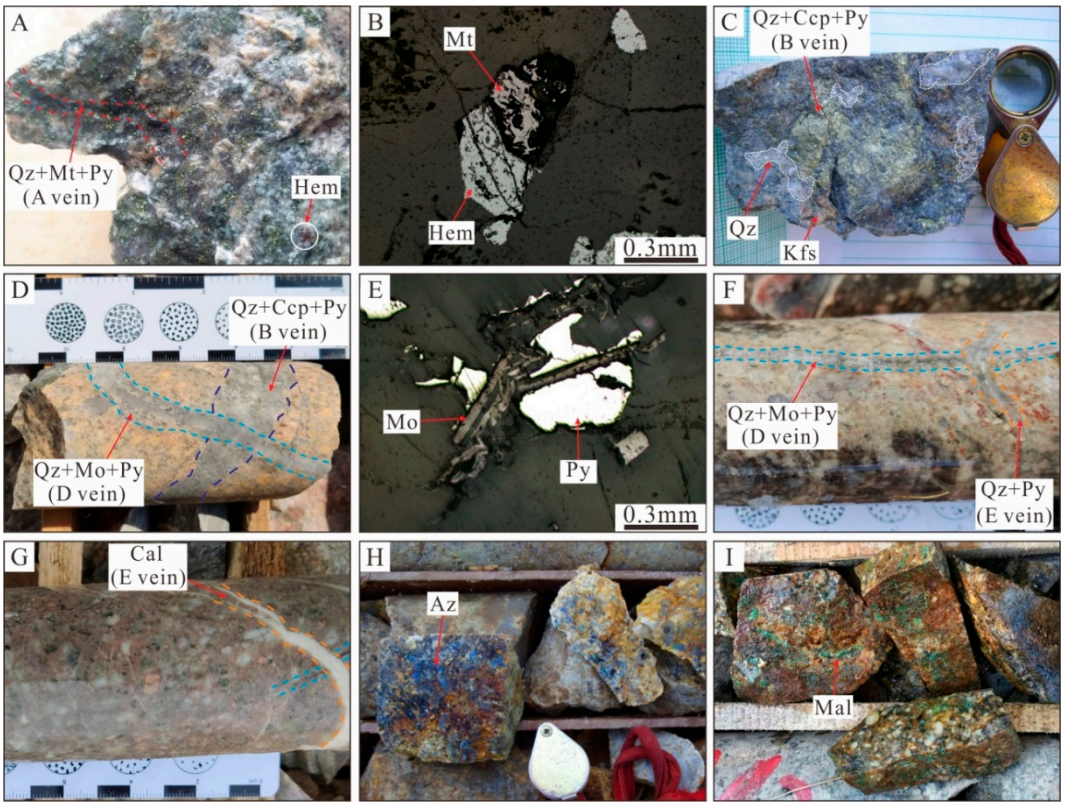

Figure 4. Photographs and photomicrographs of representative ore mineralization from the Fukeshan Cu (Mo) deposit. (**A**) Stage I quartz + magnetite + pyrite vein (A vein) in potassic-altered quartz diorite porphyry. (**B**) Anhedral magnetite and hematite in stage I. (**C**) Stage II quartz + chalcopyrite + pyrite vein (B vein) in potassic-altered quartz diorite porphyry. (**D**) Stage II quartz + chalcopyrite + pyrite vein (B vein) was crosscut by stage III quartz + molybdenite + pyrite vein (D vein). (**E**) Molybdenite intergrowth with pyrite in stage III under reflected light. (**F**) Stage III quartz + molybdenite + pyrite (D vein) vein was crosscut by stage IV quartz + pyrite vein (E vein). (**G**) Stage IV calcite vein (E vein) cutting stage III quartz vein (D vein). (**H**) The primary chalcopyrite oxidized to azurite. (**I**) The primary chalcopyrite was replaced by malachite. Abbreviations: Qz, quartz; Kfs, K-feldspar; Ser, sericite; Cal, calcite; Hem, hematite; Mt, magnetite; Py, pyrite; Ccp, chalcopyrite; Mo, molybdenite; Az, azurite; and Mal, malachite.

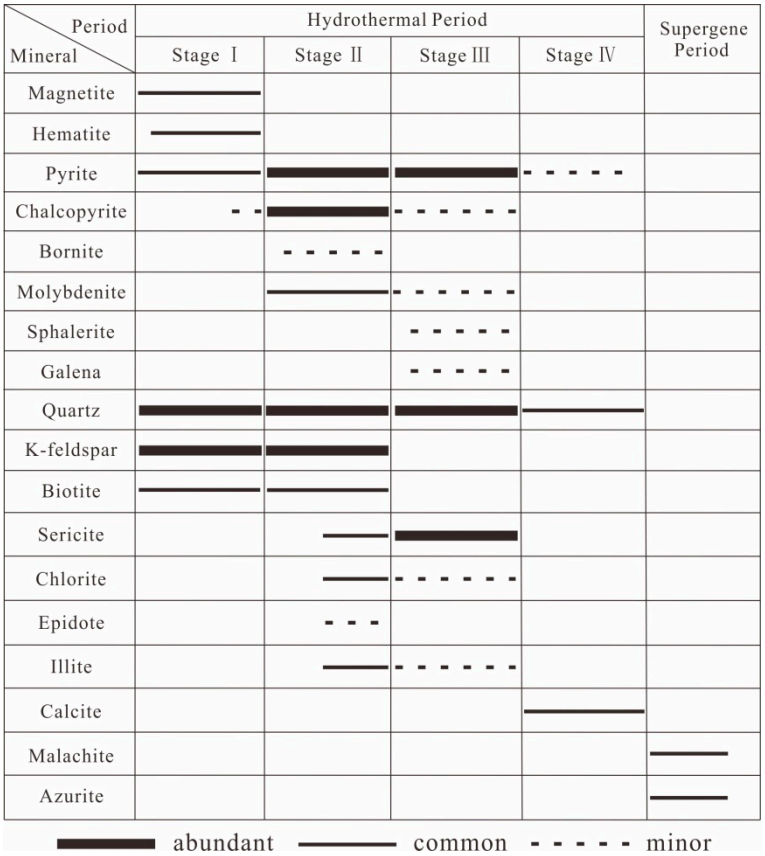

Figure 5. Paragenetic sequence of the major minerals of the Fukeshan Cu (Mo) deposit.

4. Analytical Methods

4.1. Fluid Inclusion Measurements

Fluid inclusions (FIs) petrography, laser Raman spectra, and microthermometry analyses were performed at the Key Laboratory of Mineral Resources Evaluation in Northeast Asia, Ministry of Land and Resources, Changchun, China. A total of 36 quartz samples collected from drilling operations were prepared as two-sided, 0.2 mm-thick polished sections. FIs were examined via petrographic observation under a binocular microscope, the liquid phase and the gaseous phase components of the representative FIs were analyzed using laser Raman spectroscopy by an RM-2000 laser Raman microprobe (Renishaw, New Mills, UK). The laser source is an Ar ion laser, with a wavelength of 514 nm and a laser power of 20 Mw. The laser beam width was 1 μm and the spectral resolution was 0.14 cm^{-1}. Then, the representative primary FIs were selected for microthermometric analyses. Secondary FIs were not analyzed [36]. Microthermometric analyses were conducted using a Linkam THMS-600 (Linkam Scientific Instruments Ltd., Epsom, UK) heating–freezing stage. The heating rates were generally 0.2–5.0 °C/min but were reduced to 0.2 °C/min when phase transitions were approached, and 1 °C/min when approaching FIs homogenization temperatures. The estimated precision of the measurements is ±0.1 °C for final ice melting temperatures and ±2 °C for the homogenization temperatures.

4.2. H–O Isotope Analyses

Four representative quartz samples were collected from quartz + K-feldspar + pyrite vein (stage I), quartz + chalcopyrite vein (stage II), quartz + molybdenite + pyrite vein (stage III), as well as quartz + calcite vein (stage IV). The H isotope compositions of FIs hosted in quartz samples and the O isotope compositions of quartz samples were analyzed at the Center of Analytical Laboratory in the Beijing Research Institute of Uranium Geology, China National Nuclear Corporation (CNNC).

Quartz veins from different mineralization stages were crushed to quartz grains (each 0.25–0.35 mm in size). Then quartz grains were carefully handpicked under a binocular microscope to remove visual impurities and ensure that the purity was not less than 95% and washed with double distilled water. H and O isotope compositions were analyzed using a Finnigan MAT253-EM mass spectrometer. The O isotope compositions of quartz were analyzed using the conventional BrF_5 method [37]. The H isotope compositions of FIs hosted in quartz were analyzed using the Zn reduction method [38]. The H and O isotope values were normalized with Vienna Standard Mean Ocean Water (V-SMOW) standards, with an analytical precision greater than 2‰ for δD and greater than 0.2‰ for $\delta^{18}O$.

4.3. S Isotope Analyses

Nine sulfide samples, which were collected from quartz + K-feldspar + pyrite veins (stage I), quartz + chalcopyrite ± pyrite veins (stage II), as well as quartz + molybdenite + pyrite and quartz + chalcopyrite + sphalerite + galena veins (stage III), were selected for S isotope analysis. The S isotopes of the samples were analyzed at CNNC. The individual metal sulfide mineral (purity > 99%) was mixed with cuprous oxide and powdered to 200 mesh (0.076 mm). After the samples were mixed evenly, they were heated at 980 °C under a vacuum pressure of 2×10^{-2} Pa to generate SO_2 gas. The SO_2 gas was collected by freezing in a vacuum. Then, S isotopes were analyzed using a Delta V Plus mass spectrometer. Sulfur isotope ratios are reported in the standard notation as per mil (‰) deviations from the sulfur isotope composition of the Vienna Cañon Diablo Troilite (V-CDT) standard, with an analytical precision greater than 0.2‰. The sulfide reference materials were the GBW-04414 and GBW-04415 Ag sulfide standards, with $\delta^{34}S$ values determined in this study of −0.07 ± 0.13‰ and 22.15 ± 0.14‰, respectively. And the accuracy with respect to the sulfide reference materials was greater than 99%.

4.4. Pb Isotope Analyses

Four sulfide and one quartz diorite porphyry samples were selected for Pb isotope analysis, also analyzed at CNNC. Four sulfide samples were collected from quartz + K-feldspar + pyrite vein (stage I), quartz + chalcopyrite vein (stage II), as well as quartz + molybdenite + pyrite and quartz + chalcopyrite + galena veins (stage III). Approximately 30–100 mg of powdered sample was dissolved in Teflon bombs with an ultrapure HF + HNO_3 mixture. The samples were dried after complete dissolution. The residue was then dissolved in an HBr + HNO_3 mixture and loaded into a column of AG 1-X8 anionic resin. The extracted Pb was then purified in a second column. About 100 ng of Pb was loaded onto single rhenium filaments using the silica gel technique. The Pb isotopes were analyzed with an ISOPROBE-T thermal ionization mass spectrometer, with an analytical precision greater than 0.09%. The measured Pb isotope ratios were corrected for instrumental mass fractionation of 0.11% per atomic mass unit by comparisons with repeated analyses of the standard sample (NBS-981).

4.5. Chalcopyrite Re–Os Dating

Six chalcopyrite samples, which were collected from quartz + chalcopyrite veins (stage II), were collected for Re–Os dating. Chalcopyrite grains (each 0.25–0.35 mm in size) were magnetically separated and handpicked under a binocular microscope to ensure a purity higher than 99%. The Re–Os isotope analyses were conducted at the Re–Os Isotope Laboratory, National Research Center of Geoanalysis, Chinese Academy of Geological Sciences (CAGS). The detailed procedures used here were described in [39]. The chalcopyrite standard GBW04477/JCBY [40] was used in this study to control reproducibility and instrument stability. Isoplot/Ex ver. 3.0 [41] was used to calculate the Re–Os isochron age.

5. Analytical Results

5.1. Fluid Inclusions

5.1.1. Petrography and Types of Fluid Inclusion

Petrographic studies indicated that primary fluid inclusions (FIs) in four mineralization stages were distributed regularly or randomly along growth bands in quartz crystals, and occasionally existed as isolations, showing characteristic of primary FIs [36]. Secondary FIs are usually smaller than primary FIs, and generally occur along fractures or grain boundaries in clusters and linear arrays. All FIs data collected in this study were from primary FIs. At room temperature (25 °C), three types of FIs were determined by examining their phases, filling degree, and assemblage relations. The specific characteristics of the FIs are as follows.

Liquid-rich two-phase (L-type) FIs consist of vapor and liquid water (as indicated by Raman spectroscopy) with filling degrees of 70–95 vol % (Figure 6A,C–E), in other words, the vapor phase mainly occupies 5–30 vol % of the inclusion volume. L-type FIs from stages II and III show various vapor phase proportion but display relatively constant vapor phase proportion in stages I and IV. L-type FIs generally display relatively larger vapor phase proportion (15–30 vol %) in stage I, with a few up to 45 vol % of vapor phase proportion (Figure 6A). However, L-type FIs from stage IV show relatively lower vapor phase proportion (5–15 vol %) (Figure 6E). L-type FIs range in size from 5 to 15 μm and exhibit native-crystal, irregular or round shapes. L-type FIs commonly homogenize to liquid during heating. L-type FIs are the most common type in all mineralization stages (Figure 6A,C–E).

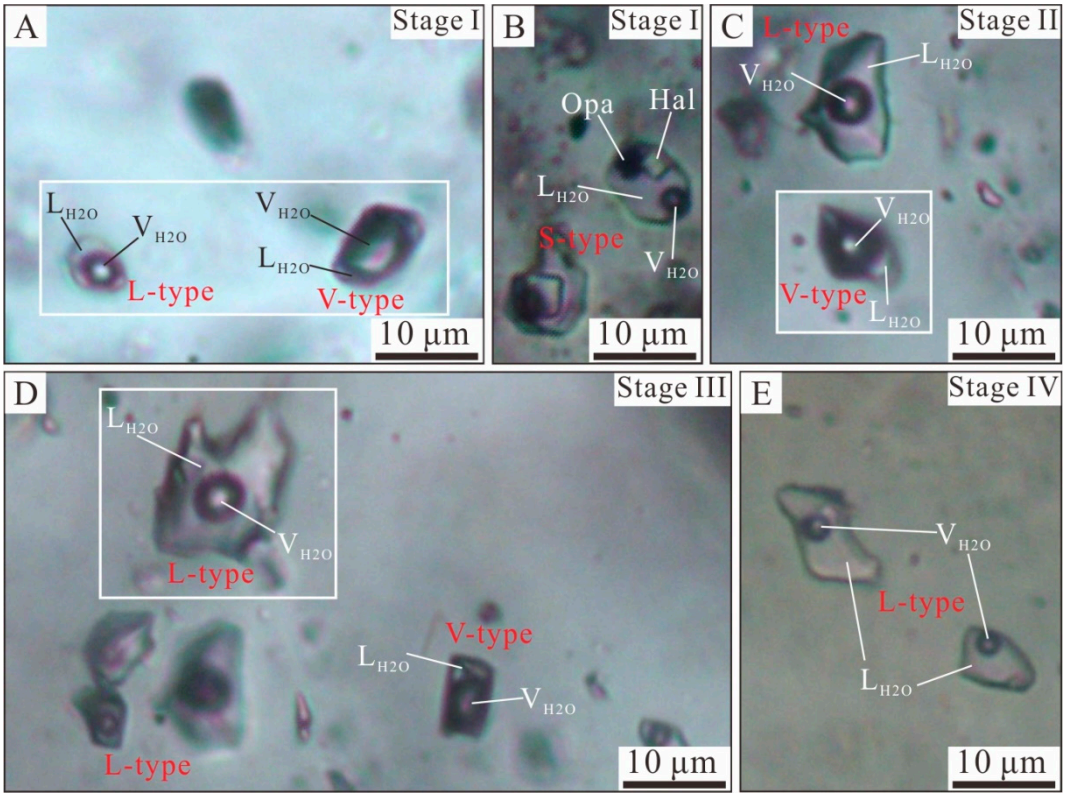

Figure 6. Photomicrographs of the representative primary fluid inclusions of different mineralization stages in the Fukeshan Cu (Mo) deposit. (**A**) The coexisting primary liquid-rich two-phase (L-type) and vapor-rich two-phase (V-type) fluid inclusions (FIs) in stage I quartz. (**B**) Daughter mineral-bearing three-phase (S-type) FIs in stage I quartz. (**C**) Primary L-type FIs coexist with V-type FIs in stage II quartz. (**D**) The coexisting primary L- and V-type FIs in stage III quartz.

(**E**) Primary L-type FIs in stage IV quartz. Abbreviations: L_{H2O} = H_2O liquid; V_{H2O} = H_2O vapor; Hal, halite; and Opa, unidentified opaque mineral.

Vapor-rich two-phase (V-type) FIs are identified in stages I, II, and III. They consist of vapor and liquid water (as indicated by Raman spectroscopy) with filling degrees of 10–30 vol %, in other words, the vapor phase generally occupies 70–90 vol % (Figure 6A,C,D). They are normally round or oval in shape and 8–16 μm in size. V-type FIs commonly homogenize to vapor during heating. V-type FIs in different stages show various vapor phase proportion (Figure 6A,C,D).

Daughter mineral-bearing three-phase (S-type) FIs are only observed in stage I, and consist of liquid, a vapor bubble, and one or more solid daughter minerals (Figure 6B). They mainly occur in irregular or oval shapes and vary from 5 to 15 μm in size, with a few up to 20 μm. The daughter minerals observed are halite and unidentified metallic minerals (Figure 6B). The halite daughter minerals are generally transparent and angular cube shapes (Figure 6B), and metallic minerals are opaque. During heating, the halite daughter minerals generally dissolved after the vapor bubble disappeared.

5.1.2. Microthermometric Results

Table 1 lists the microthermometric data for primary FIs from four different mineralization stages, which are also shown in Figure 7. The liquid phase and the gaseous phase components of S-type FIs from stage I, as well as the gaseous phase components of L- and V-type FIs from four different mineralization stages, were analyzed using laser Raman spectroscopy. The spectra indicate that the liquid and vapor phases are almost entirely H_2O (Figure 8). On freezing/warming, eutectic first melting temperatures of the FIs from stages I to III ranged from −27.9 to −23.7 °C, indicating the fluid is mainly composed of Na-chloride solutions with low concentrations of K and Mg cations [42]. However, the liquid phase of FIs from stage IV are too small to observe the eutectic temperature. According to the analysis of the eutectic temperatures, we can assume the fluids as approximating the simple H_2O–NaCl system, so we used the program HOKIEFLINCS_H_2O–NaCl to estimate the salinities of L- and V-type FIs [43]. As most S-type FIs showed homogenization by halite dissolution in the Fukeshan Cu (Mo) deposit, a direct application of halite dissolution temperature can lead to uncertainties [44,45]. Therefore, we calculated the salinities of S-type FIs according to the equations of [46].

Table 1. Microthermometric data and calculated parameters for fluid inclusions from the Fukeshan Cu (Mo) deposit.

Mineralization Stages	Host Minerals	Inclusion Types	*N*	Tm-eu (°C)	Tm-ice (°C)	Th-s (°C)	Th-v (°C)	Salinity (wt. % NaCl Equivalent)
I	Qz	L-type	42	−27.9 to −26.4	−8.2 to −4.5	-	381–477	7.2–11.9
		V-type	12	−27.0 ± 0.5	−8.0 to −5.2	-	424–471	8.1–11.7
		S-type	23		-	420–494	354–436	50.1–58.6
II	Qz	L-type	44	−27.5 to −25.1	−6.5 to −2.9	-	282–391	4.8–9.9
		V-type	17	−26.5 ± 0.5	−6.2 to −3.4	-	321–398	5.6–9.5
III	Qz	L-type	50	−25.9 to −23.7	−5.0 to −0.8		233–340	1.4–7.9
		V-type	19	−25.0 ± 0.5	−4.0 to −1.5	-	261–334	2.6–6.4
IV	Qz	L-type	39		−2.3 to −0.5		144–239	0.9–3.9

Tm-eu = eutectic temperature (first ice melting temperature); Tm-ice = temperature of final ice melting; Th-s = dissolution temperature of halite; Th-v = homogenization temperature of V-type or L-type FIs, vapor disappearance temperature of S-type FIs; and Qz = quartz.

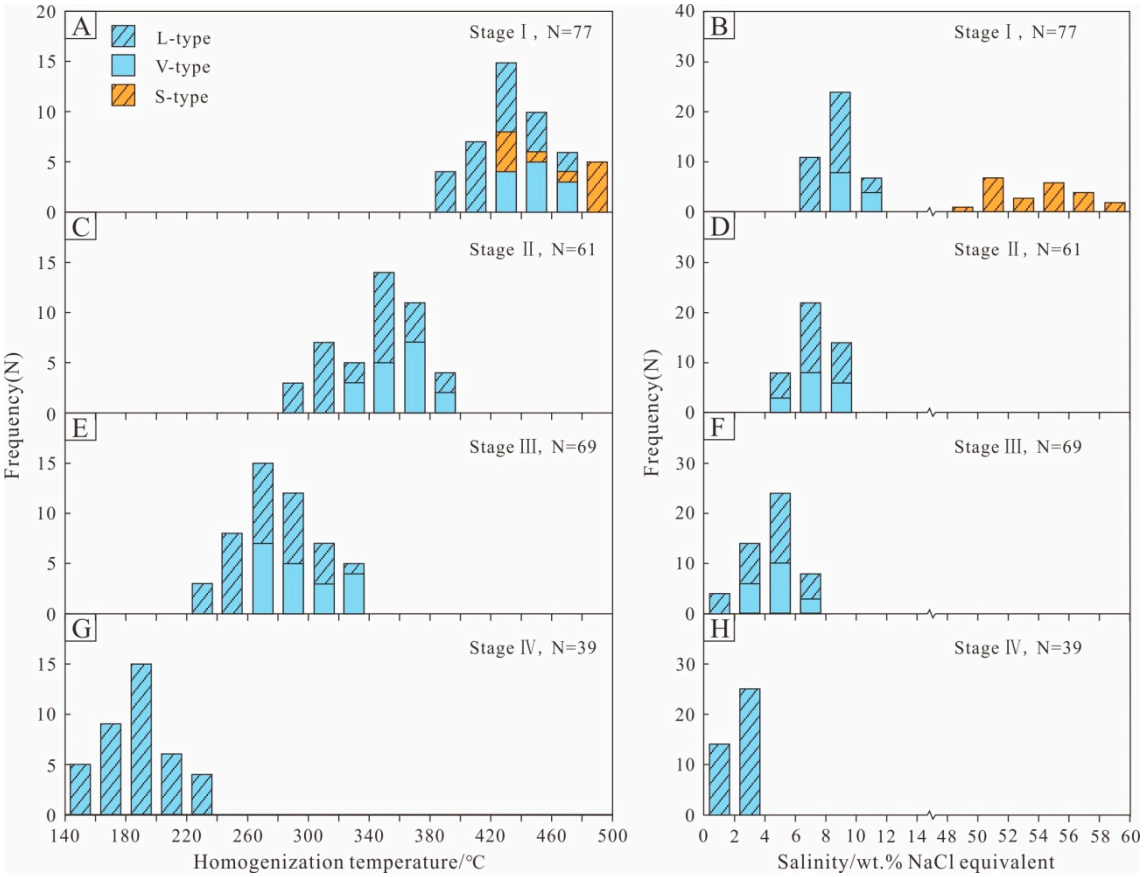

Figure 7. Frequency histograms of homogenization temperatures and salinities for fluid inclusions (FIs) in the Fukeshan Cu (Mo) deposit. (**A**) Homogenization temperatures histogram for L-, V-, and S-type FIs from stage I quartz; (**B**) Salinities histogram for L-, V-, and S-type FIs from stage I quartz; (**C**) Homogenization temperatures histogram for L- and V-type FIs from stage II quartz; (**D**) Salinities histogram for L- and V-type FIs from stage II quartz; (**E**) Homogenization temperatures histogram for L- and V-type FIs from stage III quartz; (**F**) Salinities histogram for L- and V-type FIs from stage III quartz; (**G**) Homogenization temperatures histogram for L-type FIs from stage IV quartz; (**H**) Salinities histogram for L-type FIs from stage IV quartz.

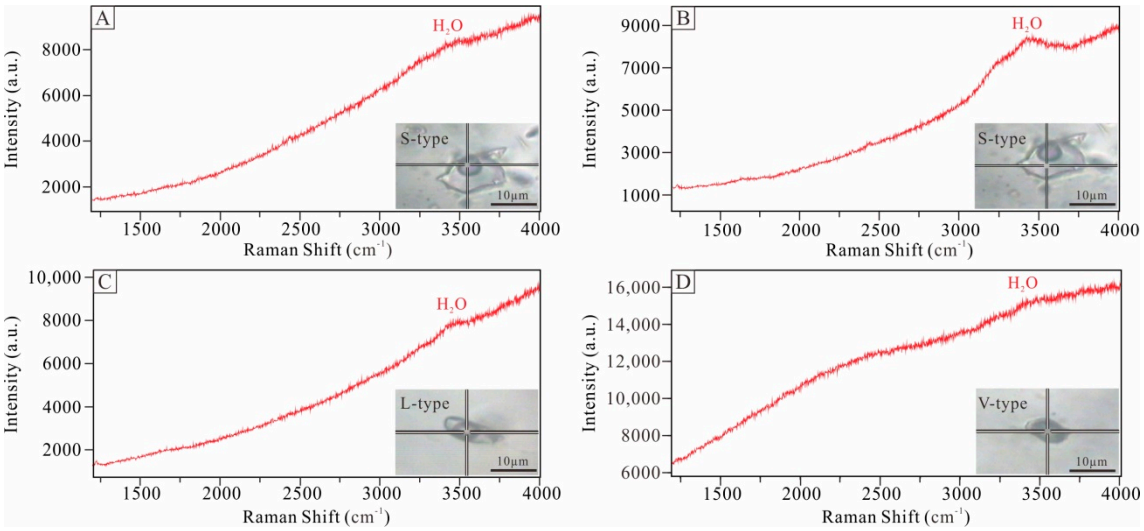

Figure 8. Representative Laser Raman spectra for different types of fluid inclusions. (**A**) The vapor phases of S-type FIs are almost entirely H_2O; (**B**) The liquid phases of S-type FIs are almost entirely H_2O; (**C**) The vapor phases of L-type FIs are almost entirely H_2O; (**D**) The vapor phases of V-type FIs are almost entirely H_2O.

We observed L-, V-, and S-type FIs in stage I quartz grains (Figure 6A,B). During heating, all L-type FIs homogenized to an aqueous liquid phase at 381–477 °C (n = 42), peaking at 420–440 °C (Figure 7A). These L-type FIs yielded $T_{m\text{-}ice}$ of −8.2 to −4.5 °C, corresponding to salinities of 7.2–11.9 wt. % NaCl equivalent (n = 42), concentrated between 8 and 10 wt. % NaCl equivalent (Figure 7B). The V-type FIs homogenized to a vapor phase at 424–471 °C (n = 12) (Figure 7A), yielding $T_{m\text{-}ice}$ of −8.0 to −5.2 °C, with calculated salinities of 8.1 to 11.7 wt. % NaCl equivalent (n = 12) (Figure 7B). S-type FIs homogenized to an aqueous liquid phase during the heating process, with $T_{h\text{-}s}$ varying from 420 to 494 °C (n = 23) after vapor bubble disappearance at temperatures varying from 354 to 436 °C (n = 23) (Figure 7A). The salinities are estimated to range from 50.1 to 58.6 wt. % NaCl equivalent (n = 23) (Figure 7B).

We observed L-, and V-type FIs in stage II quartz grains (Figure 6C). During heating, all L-type FIs homogenized to the aqueous liquid phase at 282–391 °C (n = 44), peaking at 340–360 °C (Figure 7C). These L-type FIs yielded $T_{m\text{-}ice}$ ranging from −6.5 to −2.9 °C, corresponding to salinities from 4.8–9.9 wt. % NaCl equivalent (n = 44), concentrated between 6 and 8 wt. % NaCl equivalent (Figure 7D). The V-type FIs homogenized to the vapor phase at 321–398 °C (n = 17) (Figure 7C). They yielded $T_{m\text{-}ice}$ ranging from −6.2 to −3.4 °C, with calculated salinities of 5.6 to 9.5 wt. % NaCl equivalent (n = 17) (Figure 7D).

We observed L-, and V-type FIs in stage III quartz grains (Figure 6D). During heating, all L-type FIs homogenized to the aqueous liquid phase at 233–340 °C (n = 50), peaking at 260–280 °C (Figure 7E). These L-type FIs yielded $T_{m\text{-}ice}$ ranging from −5.0 to −0.8 °C, corresponding to salinities of 1.4–7.9 wt. % NaCl equivalent (n = 50), concentrated between 4 and 6 wt. % NaCl equivalent (Figure 7F). The V-type FIs homogenized to the vapor phase at 261–334 °C (n = 19) (Figure 7E). They yielded $T_{m\text{-}ice}$ varying from −4.0 to −1.5 °C, with calculated salinities of 2.6 to 6.4 wt. % NaCl equivalent (n = 19) (Figure 7F).

Only the L-type FIs were observed in stage IV quartz crystals (Figure 6E). They were homogenized to an aqueous liquid phase at 144–239 °C (n = 39), peaking at 180–200 °C (Figure 7G). These L-type FIs in this stage yielded $T_{m\text{-}ice}$ ranging from −2.3 to −0.5 °C, corresponding to salinities of 0.9 to 3.9 wt. % NaCl equivalent (n = 39), concentrated between 2 and 4 wt. % NaCl equivalent (Figure 7H).

5.2. H–O Isotopes

The H and O analytical results are listed in Table 2 and shown in Figure 9. The measured $\delta^{18}O_{V\text{-}SMOW}$ values of four quartz samples from four mineralization stages range from 6.2 to 9.0‰. The quartz–water equilibrium equation was used to calculate the $\delta^{18}O_{H2O}$ values ($1000\ln\alpha_{quartz\text{–}water} = 3.38 \times 10^6/T^2 - 3.4$) [47]. The calculated $\delta^{18}O_{H2O}$ values from stages I to IV are 5.6‰, 1.2‰, −1.0‰, and −6.2‰, respectively (Table 2). The measured δD values of FIs in quartz from stages I to IV are −109.9‰, −125.7‰, −140.9‰, and −152.3‰, respectively (Table 2).

Table 2. H and O isotope data for fluids in quartz from the Fukeshan Cu (Mo) deposit.

Sample No.	Mineral	Mineralization Stages	Sample Description	$\delta^{18}O_{V\text{-}SMOW}$ (‰)	T (°C)	$\delta^{18}O_{H2O}$ (‰)	δD (‰)
FKS-ZK4002-HO1	Quartz	I	Qz + Kf + Py vein	9.0	430	5.6	−109.9
FKS-ZK4002-HO2	Quartz	II	Qz + Ccp vein	6.5	350	1.2	−125.7
FKS-ZK4002-HO3	Quartz	III	Qz + Mo + Py vein	7.1	270	−1.0	−140.9
FKS-ZK4002-HO4	Quartz	IV	Qz + Cal vein	6.2	190	−6.2	−152.3

$\delta^{18}O_{H2O}$ of water in equilibrium with quartz were calculated according to the equation of $1000\ln\alpha_{quartz-water} = 3.38 \times 10^6/T^2 - 3.4$ [47], which were defined by the peak homogenization temperatures (T) of fluid inclusions for corresponding quartz samples. Abbreviations: Ccp = chalcopyrite, Kf = K-feldspar, Mo = molybdenite, Py = pyrite, Qz = quartz, and Cal = calcite.

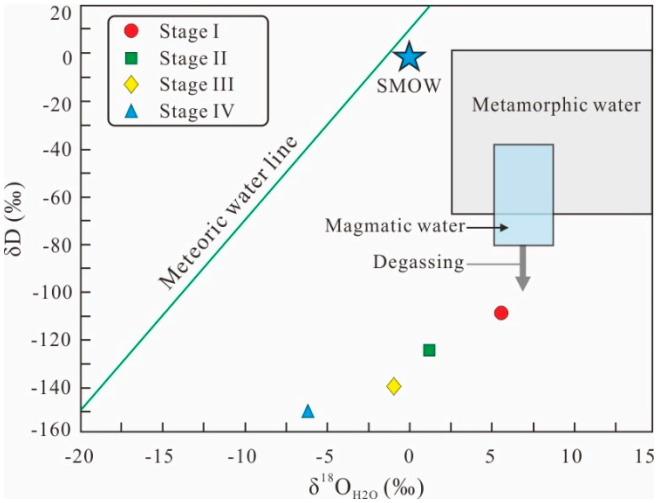

Figure 9. Plots of δD vs. $\delta^{18}O_{H2O}$ for the ore-forming fluids of the Fukeshan Cu (Mo) deposit. Diagram is from [48]. SMOW = Standard Mean Ocean Water.

5.3. S–Pb Isotopes

Table 3 lists the S isotope compositions of nine sulfide samples (including pyrite, chalcopyrite, molybdenite, sphalerite, and galena) from mineralization stages I to III in the Fukeshan deposit, which are shown in Figure 10. The $\delta^{34}S_{V-CDT}$ values of the sulfides from mineralization stages I to III range from 3.3‰ to 3.4‰, −2.3‰ to 1.7‰, and 0.3‰ to 1.1‰, respectively (Table 3).

Table 3. S isotope data of sulfide minerals from the Fukeshan Cu (Mo) deposit.

Sample No.	Mineral	Mineralization Stages	Sample Description	$\delta^{34}S_{V-CDT}$
FKS-ZK4002-S1	Pyrite	I	Qz + Kf + Py vein	3.4
FKS-ZK4002-S2	Pyrite	I	Qz + Kf + Py vein	3.3
FKS-ZK4002-S3	Chalcopyrite	II	Qz + Ccp vein	−1.5
FKS-ZK4002-S4	Chalcopyrite	II	Qz + Ccp vein	−2.3
FKS-ZK4002-S5	Pyrite	II	Qz + Ccp + Py vein	1.7
FKS-ZK4001-S1	Molybdenite	III	Qz + Mo + Py vein	0.6
FKS-ZK4001-S2-1	Sphalerite	III	Qz + Ccp + Sp + Gn vein	1
FKS-ZK4001-S2-2	Galena	III	Qz + Ccp + Sp + Gn vein	0.3
FKS-ZK4001-S3	Pyrite	III	Qz + Mo + Py vein	1.1

Abbreviations: Ccp = chalcopyrite, Kf = K-feldspar, Mo = molybdenite, Py = pyrite, Sp = Sphalerite, Gn = Galena, and Qz = quartz.

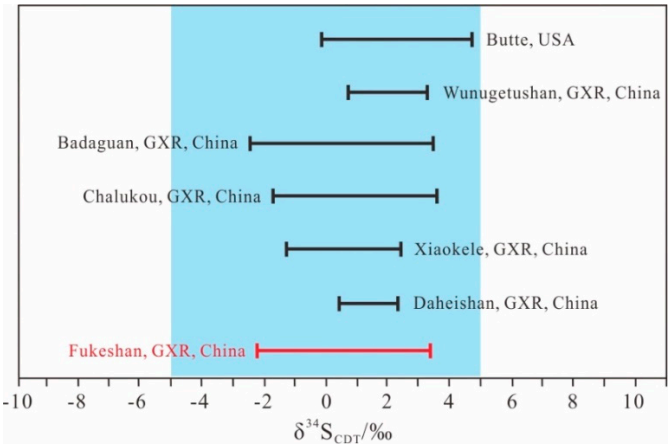

Figure 10. Comparison of the Fukeshan Cu (Mo) deposit S isotope compositions with other typical porphyry Cu deposits worldwide [49–54].

Table 4 lists the Pb isotope compositions of four sulfide samples (including pyrite, chalcopyrite, molybdenite, and galena) from mineralization stages I to III in the Fukeshan deposit, which are plotted in Figure 11. The Pb isotope compositions of the sulfides have limited variation in their $^{206}Pb/^{204}Pb$, $^{207}Pb/^{204}Pb$ and $^{208}Pb/^{204}Pb$ ratios, i.e., 18.408 to 18.452, 15.590 to 15.607, and 38.376 to 38.382, respectively.

Table 4. Pb isotope ratios of sulfide samples from the Fukeshan Cu (Mo) deposit.

Sample No.	Mineral	Mineralization Stages	Sample Description	$^{206}Pb/^{204}Pb$	Error	$^{207}Pb/^{204}Pb$	Error	$^{208}Pb/^{204}Pb$	Error
FKS-ZK4001-Pb1	Pyrite	I	Qz + Kf + Py vein	18.449	0.002	15.590	0.002	38.376	0.004
FKS-ZK4001-Pb2	Chalcopyrite	II	Qz + Ccp vein	18.408	0.002	15.607	0.002	38.380	0.005
FKS-ZK4002-Pb1	Molybdenite	III	Qz + Mo + Py vein	18.445	0.002	15.590	0.002	38.382	0.006
FKS-ZK4002-Pb2	Galena	III	Qz + Ccp + Gn vein	18.452	0.003	15.604	0.003	38.382	0.007
FKS-ZK4001-Pb3	Quartz diorite porphyry			18.228	0.002	15.572	0.002	38.207	0.004

Abbreviations: Qz = quartz, Kf = K-feldspar, Ccp = chalcopyrite, Mo = molybdenite, and Gn = Galena.

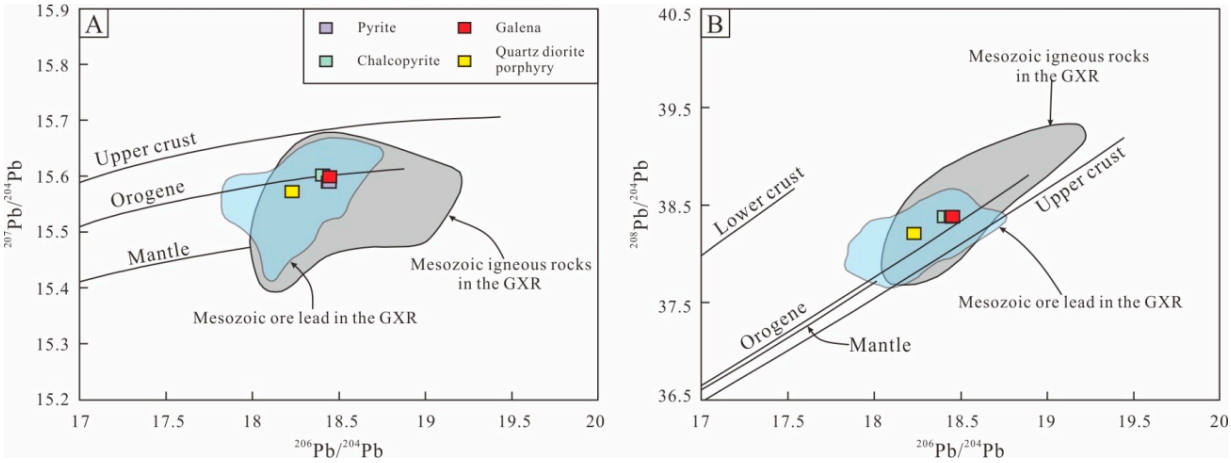

Figure 11. Lead isotopic compositions of sulfides and quartz diorite porphyry in the Fukeshan Cu (Mo) deposit. (**A**) $^{207}Pb/^{204}Pb$ vs. $^{206}Pb/^{204}Pb$. (**B**) $^{208}Pb/^{204}Pb$ vs. $^{206}Pb/^{204}Pb$. The evolution line of mantle, orogene, and the lower and upper crust reservoirs are from [55]. Pb isotope data for Late Jurassic–

Early Cretaceous ore in the GXR are from [51,52,56]. Pb isotope data for Mesozoic igneous rocks in the GXR are from [57].

5.4. Chalcopyrite Re–Os Dating

Table 5 presents the Re–Os isotope compositions of six chalcopyrite samples from mineralization stage II in the Fukeshan deposit. The concentrations of Re and common Os in the samples range from 0.4177 to 3.7997 ng/g and from 0.0021 to 0.0515 ng/g, respectively. Their $^{187}Re/^{188}Os$ values range from 130 to 5997, and their $^{187}Os/^{188}Os$ ratios range from 0.738 to 15.1. The data for the six chalcopyrite samples yielded an isochron age of 144.7 ± 5.4 Ma (MSWD = 3.8, initial $^{187}Os/^{188}Os$ = 0.45 ± 0.05; Figure 12), which represents the Cu mineralization age of the Fukeshan Cu (Mo) deposit.

Table 5. Re–Os dating results of chalcopyrite from the Fukeshan Cu (Mo) deposit.

Sample No.	Weight (g)	Re (ng/g)		Common Os (ng/g)		$^{187}Re/^{188}Os$		$^{187}Os/^{188}Os$	
		Measured	Error	Measured	Error	Measured	Error	Measured	Error
ZK4002-Re-Os1	0.0317	0.4177	0.0048	0.0156	0.0001	130	1.81	0.738	0.005
ZK4002-Re-Os2	0.0244	3.3842	0.0283	0.0021	0.0001	5997	93.7	15.1	0.209
ZK4002-Re-Os3	0.0361	1.9076	0.0165	0.0347	0.0003	266	3.16	1.12	0.011
ZK4001-Re-Os1	0.0198	1.6770	0.0180	0.0041	0.0001	2133	21.9	5.52	0.053
ZK4001-Re-Os2	0.0268	1.8857	0.0165	0.0515	0.0005	177	2.15	0.861	0.014
ZK4001-Re-Os3	0.0242	3.7997	0.0299	0.0436	0.0004	420	4.84	1.48	0.014

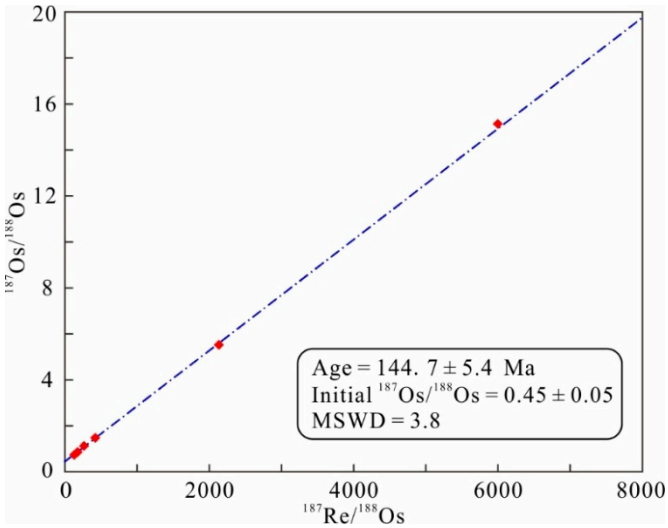

Figure 12. Chalcopyrite Re–Os isotope isochron diagram from the Fukeshan Cu (Mo) deposit. MSWD = mean square weighted deviation, a measure of scatter.

6. Discussion

6.1. Timing of Cu (Mo) Mineralization

The ore bodies in the Fukeshan deposit are mainly hosted within the quartz diorite porphyries (Figure 2B). Geochronology data indicate that chalcopyrite Re–Os isochron age (144.7 ± 5.4 Ma) corresponds well with the zircon U–Pb weighted mean age of the Fukeshan quartz diorite porphyry (148.7 ± 0.8 Ma) [22], indicating that the quartz diorite porphyry and Cu mineralization in the Fukeshan Cu (Mo) deposit occurred contemporaneously. In recent years, the Late Jurassic porphyry Cu (Mo) mineralization events have been increasingly reported in the northern GXR, such as the Chalukou porphyry Mo deposit (148 ± 1 Ma) [17], the Xiaokele porphyry Cu (Mo) deposit (150.0 ± 1.6) [19], and the Daheishan (147 ± 2 Ma) porphyry Cu (Mo) deposit [18]; these results indicate that Late Jurassic was a crucial time for porphyry Cu (Mo) mineralization in the northern GXR.

6.2. Source of the Ore-Forming Materials

The $\delta^{34}S$ values of sulfides from mineralization stages I to III in the Fukeshan Cu (Mo) deposit have a narrow range of −2.3‰ to 3.4‰ (Table 3; Figure 10), reflecting a remarkably homogeneous sulfur source. There are no sulphate minerals in the Fukeshan Cu (Mo) deposit, which indicates weak sulfur fractionation in various valence states during different mineralization stages. The $\delta^{34}S$ values are near 0‰, indicating a magmatic source and are interpreted to reflect uniformity of the ore-forming fluids (−5‰ to 5‰) [58]. The $\delta^{34}S$ values of the sulfides in the Fukeshan deposit overlap with those of typical porphyry deposits in the world (Figure 10) [59], such as Butte porphyry Cu–Mo deposit in USA (−0.1‰ to 4.7‰) [50], Wunugetushan (0.76‰ to 3.20‰) [53], and Badaguan (−2.4‰ to 3.5‰) [54]. In addition, the $\delta^{34}S$ values of the sulfides in the Fukeshan deposit match the sulfur isotope compositions of Late Jurassic porphyry deposits in the northern GXR, such as Chalukou Mo (−1.9‰ to 3.6‰) [52], Xiaokele Cu (Mo) (−1.2‰ to 2.4‰; our unpublished data), and Daheishan Cu (Mo) (0.4‰ to 2.3‰) [51] (Figure 10). All of these deposits have sulfur origins from Late Jurassic intermediate-acid porphyries (150–147 Ma). Considering the intrusive magmatic activities and the chalcopyrite Re–Os isochron age (144.7 ± 5.4 Ma) in the Fukeshan deposit, we suggest that the sulfur in the ores was most likely derived from Late Jurassic intrusive rocks.

In order to further evaluate the metal source, we made use of previously published Pb isotope data, including Pb isotope data for Mesozoic ore in the GXR [51,52,56], and Pb isotope data for Mesozoic igneous rocks in the GXR [57] (Figure 11). The Pb isotope ratios of Mesozoic igneous rocks in the GXR are mainly distributed between upper crust and mantle values, implying a mixed source [58] (Figure 11). Significantly, the Pb isotope ratios of Mesozoic ore in the GXR plot in the lead region of Mesozoic igneous rocks, suggesting that the source of ore lead was most likely related to Mesozoic igneous rocks. Likewise, Pb isotope data from the Fukeshan deposit all plot in the lead region of an orogenic belt between upper crust and mantle sources, indicating that Pb was most likely derived from a deep-seated magma that involved some crustal materials [54]. Pb isotope ratios of the sulfides from different mineralization stages in the Fukeshan deposit are uniform, suggesting the hydrothermal fluids were derived from a well-mixed and homogeneous magma [59]. We have obtained only one set of Pb isotope data for the quartz diorite porphyry from the Fukeshan deposit, but Pb isotope compositions of the quartz diorite porphyry do not overlap with those of sulfides well (Figure 11). Even so, in the Fukeshan deposit, the Pb isotope ratios of the sulfides and the quartz diorite porphyry plot in the lead region of Mesozoic ore and igneous rocks in the GXR (Figure 11), suggesting that the Pb isotope compositions of the sulfides and the quartz diorite porphyry may have shared a common Pb source with the Mesozoic igneous rocks in the GXR. Considering Late Jurassic ore-bearing intrusive rocks and mineralization age (chalcopyrite Re–Os isochron age of 144.7 ± 5.4 Ma) in the Fukeshan deposit, we suggest that the lead and ore-forming metals were most likely derived from Late Jurassic intrusive rocks.

6.3. Fluid Immiscibility and Pressure Estimates

In the Fukeshan deposit, fluid immiscibility most likely happened in stage I, supported by the following evidence (1) S-type and V-type FIs coexisting in the same quartz crystal show close genetic relationship, and (2) S-type and V-type FIs display similar homogenization temperatures but contrasting salinities (Figure 7A,B). Trapping pressure can be accurately estimated when the fluid immiscibility was occurring in the fluid system at the capture time [60]. Considering the evidence of fluid immiscibility in stage I, based on the simple H_2O–NaCl system, trapping pressures in stage I are estimated to range from ~200 to ~500 bar (Figure 13) using the isobar equations reported in [61].

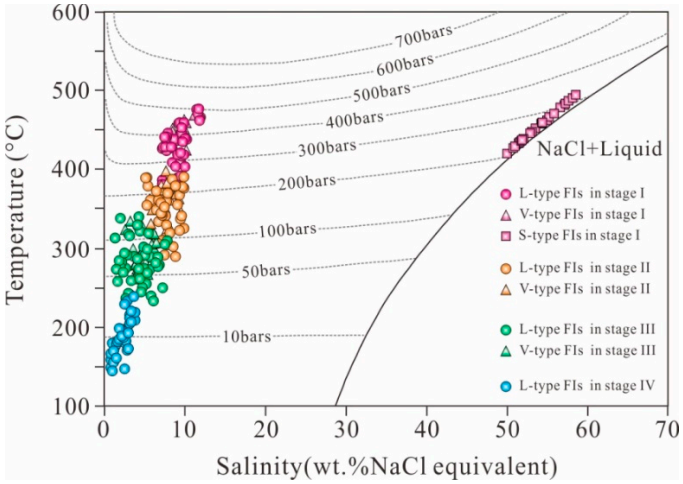

Figure 13. Pressure estimation for fluid inclusions of different mineralization stages in the Fukeshan Cu (Mo) deposit. Isobars were calculated from the equations of [61].

L-type and V-type FIs assemblage from stages II to IV are not the real immiscibility assemblage in porphyry systems and they are not suitable to estimate the accurate trapping pressure conditions. Pressures obtained for such assemblage can only represent minimum trapping values [62]. Based on the simple H_2O–NaCl system, using the isobar equations reported in [61], we estimate the minimum trapping pressures in stages II and III range from ~70 to ~300 bar and ~30 to ~150 bar, respectively (Figure 13). The minimum trapping pressures in stage IV occurred at pressures <50 bar (Figure 13).

6.4. Origin and Evolution of the Ore-Forming Fluids

FIs provide a record of ore-forming fluid systems, and investigations of FIs can yield certain indications as to the nature and genesis of the original fluids [36,63]. The $\delta^{18}O_{H2O}$ values for stage I veins (5.6‰) are similar to magmatic water values [51], suggesting that the ore-forming fluids from the early stage derived from a magmatic source, but the δD values (−109.9‰) of the ore-forming fluids in stage I are obviously lower than typical magmatic water values (Figure 9) [64]. Previous studies have suggested that the low δD values in most porphyry deposits may be due to magma degassing and fluid boiling [65–67]. During the late crystallization period, continuous degassing of parent magma in an open system would reduce the δD values of the residual water with little influence on the $\delta^{18}O_{H2O}$ values [68,69]. Furthermore, fluid boiling occurred in stage I, vapor separation caused by fluid boiling would also decrease the δD values in the remaining ore-forming fluids [70]. Therefore, the low δD values in stage I are likely a consequence of magma degassing and fluid boiling. In addition, previous studies have also shown that such depleted δD isotope values are widely recorded by ore-forming fluids in the early stage of other porphyry deposits in the GXR [7], such as the Hashitu porphyry Mo deposit [71], Wulandele porphyry Mo deposit [72], and Chalukou porphyry Mo deposit [55], which likely have a predominantly magmatic origin. The samples from stages II to IV display relatively lower δD and $\delta^{18}O_{H2O}$ values than those from stage I, plot in the region between the meteoric water line and the magmatic water field (Figure 9), this indicates the involvement of meteoric water. In addition, ore-forming fluids from stages II to IV have characteristics of middle-low salinities and are different from typical exsolved magmatic fluids, which are characterized by high temperature and high salinity [73]. This also implies that meteoric water may be involved in the ore-forming fluids, especially in the late stage. In addition, the bulk fluid inclusion decrepitation method, which was employed to provide the water for the δD analyses, inevitably led to sampling a mixture of primary and secondary fluid inclusions, resulting in the low δD values from stages I to IV.

The development of the L-, V- and S-type FIs in stage I hydrothermal quartz suggests that the initial hydrothermal fluids are characterized by high homogenization temperatures and high salinities (Figure 7A,B). Observations of mineral association, such as hematite and magnetite

(Figure 4A,B), but rare sulfides in stage I veinlets, indicate highly oxidized initial hydrothermal fluids [74], typical features of porphyry-type deposits [75,76]. Because of the high oxygen fugacity, the sulfur within the magma was mostly present as sulfate [53,77]. Sulfide mineralization, however, was inevitably constrained as sulfur in ore minerals, mainly existing in the reduced form of S^{2-}, although fluid boiling may have occurred in stage I. L- and V-type FIs were observed in quartz crystals from stages II and III (Figure 6C,D). Compared with stage I, hematite and magnetite were not observed in stages II and III, indicating that the oxygen fugacity of the fluids was distinctly lower than in stage I. Most of the stage IV quartz crystals contain single L-type FIs (Figure 6E), where the ore-forming fluids belonged to an homogeneous H_2O–NaCl system with medium-low temperature (144–239 °C) and low salinity (0.9–3.9 wt. % NaCl equivalent). This implies that the fluids in stage IV were more diluted and cooled due to a large amount of meteoric water flow during stage IV. This conclusion is consistent with results of H–O isotope compositions in this study.

6.5. Mechanism for Cu Transportation and Precipitation

Most researchers have proposed that the transportation of metals mainly occurs as complexes in aqueous liquids [64,78–80]. Cu transportation process is still a controversial issue although much research has been done on it. Most studies believe that Cu exists as chlorine complex and migrates in the brine phase [78,80]. However, many LA-ICP-MS (laser ablation-inductively coupled plasma-mass spectrometry) analysis and simulation experiments also supported that Cu is preferentially partitioned into the vapor phase rather than brine by diffusion [81–83]. In this study, most sulfide minerals are present in the S-type FIs rather than high vapor–liquid ratio FIs during different mineralization stages, indicating that Cu chloride complexes are the predominant species in the brine phase.

As described above, the initial hydrothermal fluids in stage I have high oxygen fugacity in the Fukeshan deposit. In contrast, stage II is the main Cu mineralization stage in the Fukeshan deposit, which is demonstrated to be relatively less oxidizing. A decrease in the oxygen fugacity could have resulted from either CO_2-escape that was effectively caused by fluid boiling [84–86] and/or magnetite crystallization [87–89]. Our results show that the fluid system is not a CO_2-rich system. Thus, the unmixing between water and CO_2 may not have been an important process in the Fukeshan deposit. As a result, magnetite precipitation in stage I could have led to the reduction of S^{6+} to S^{2-} ($12[FeO] + H_2SO_4 = 4Fe_3O_4 + H_2S$) [77,89], providing suitable condition for significant sulfide mineralization [89]. In this study, two main mechanisms have been proposed as the effective agents in the Cu precipitation in the Fukeshan deposit. The first factor is that Cu solubility (as chloride complex) decreases dramatically with decline of temperatures [90–92]. FIs studies show that homogenization temperatures decrease from 381–494 °C in stage I to 282–398 °C in stage II in the Fukeshan deposit (Table 1). In addition, Pb–Zn mainly precipitate in stage III with homogenization temperatures vary from 233 to 340 °C (Table 1), but only a small amount of Cu precipitate in this temperature interval. The homogenization temperatures range in the main Cu mineralization stage (stage II) are consistent with the most favorable temperature interval (~400–300 °C) for Cu precipitation in porphyry systems [90–94]. These temperature conditions are also in agreement with the thermodynamic calculations of the chloride complex in the Sungun porphyry Cu deposit (northwestern Iran) [93]. Furthermore, previous research has found that the Cu solubility in aqueous fluids was approximately 50,000 ppm at higher temperatures (~450 °C) and dropped sharply to approximately 50 ppm at about 360 °C [93]. Therefore, fluid cooling may play a very important role in precipitation of Cu precipitation in the Fukeshan deposit. In addition, decrease in temperature has a major effect on the disproportionation of SO_2 to H_2S and H_2SO_4 ($4SO_2 + 4H_2O \rightarrow 3H_2SO_4 + H_2S$) [95,96]. The disproportionation reaction is only effective below 400 °C [97]. This reaction resulted in an increase in the reduced S species (H_2S) in the fluids, which can decrease the solubility of chalcopyrite and trigger Cu precipitation [93,98–100]. The second factor is fluid mixing between magmatic fluids and meteoric water, which has long been thought to effectively lead to the deposition of metals from ore solutions [101]. Combined with the H–O isotope data in

this study, it can be concluded that the mixing between magmatic fluids and meteoric water has occurred since stage II. In addition, from stages II to IV, the salinities of the ore-forming solutions decrease with the decreasing of temperature, indicating the input of meteoric water with low-salinities and low-temperatures [102]. Fluid mixing would decrease chloride ion concentration of the ore-forming fluid, thus destabilizing the chloride complex of Cu and depositing Cu [93]. Incursions of cooler meteoric water into the magmatic fluids may have also assisted in the temperature decrease and further promoted Cu precipitation, as discussed already.

7. Conclusions

(1) The Fukeshan Cu (Mo) deposit is a typical porphyry deposit in the northern GXR. Its ore-forming process can be divided into sulfide-barren quartz veins (A vein; stage I), quartz + chalcopyrite + pyrite veins (B vein; stage II), quartz + polymetallic sulfide veins (D vein; stage III), and barren quartz + carbonate ± pyrite veins (E vein; stage IV), with Cu mineralization mainly occurred in stage II.

(2) Microthermometry of the FIs and H–O isotope data suggest that the ore-forming fluids were magmatic in origin and were gradually mixed with meteoric water from stages II to IV. Sulfur and lead isotopic results indicate that the ore-forming materials of the Fukeshan Cu (Mo) deposit were likely to originate from Late Jurassic intrusive rocks.

(3) Fluid cooling and incursions of meteoric water into the magmatic fluids were two important factors for Cu precipitation in the Fukeshan Cu (Mo) deposit.

(4) Late Jurassic quartz diorite porphyry and Cu mineralization occurred contemporaneously in the Fukeshan Cu (Mo) deposit.

Author Contributions: Conceptualization, Y.-g.S., B.-l.L., and Q.-f.D.; software, Y.Q., C.-k.W., L.-l.W., and Q.-l.X.; investigation, Y.-g.S., B.-l.L., Q.-f.D., Y.Q., and C.-k.W.; data curation, L.-l.W. and Q.-l.X.; funding acquisition, B.-l.L.; project administration, B.-l.L.; writing—original draft preparation, Y.-g.S.; and writing—review and editing, Y.-g.S. and B.-l.L. All authors have read and agreed to the published version of the manuscript.

Funding: This research was funded by the National Natural Science Foundation of China (41272093), the National Key R&D Program of China (2017YFC0601304), Natural Science Foundation of Jilin Province (No.20180101089JC), Key Projects of Science and Technology Development Plan of Jilin Province (No.20100445), Self-determined Foundation of Key Laboratory of Mineral Resources Evaluation in Northeast Asia, Ministry of Natural Resources (DBY-ZZ-19-04), and the Heilongjiang Research Project of Land and Resources (201605 and 201704).

Acknowledgments: We would like to thank staffs of the Qiqihaer Institute of Geological Exploration, Heilongjiang, China for sample collection.

Conflicts of Interest: The authors declare no conflict of interest.

Reference

1. Article Jahn, B.M.; Wu, F.Y.; Chen, B. Granitoids of the Central Asian Orogenic Belt and continental growth in the Phanerozoic. *Earth Environ. Sci. Trans. R. Soc.* **2000**, *91*, 181–193.
2. Xu, W.L.; Ji, W.Q.; Pei, F.P.; Meng, E.; Yu, Y.; Yang, D.B.; Zhang, X.Z. Triassic volcanism in eastern Heilongjiang and Jilin provinces, NE China: Chronology, geochemistry, and tectonic implications. *J. Asian Earth Sci.* **2009**, *34*, 392–402.
3. Xiao, W.J.; Santosh, M. The western Central Asian Orogenic Belt: A window to accretionary orogenesis and continental growth. *Gondwana Res.* **2014**, *25*, 1429–1444.
4. Jahn, B.M.; Windley, B.; Natal'in, B.; Dobretsov, N. Phanerozoic continental growth in Central Asia. *J. Asian Earth Sci.* **2004**, *23*, 599–603.
5. Wilhem, C.; Windley, B.F.; Stampfli, G.M. The Altaids of Central Asia: A tectonic and evolutionary innovative review. *Earth Sci. Rev.* **2012**, *113*, 303–341.
6. Song, B.J.; Wang, X.Y.; Ma, J. Characteristics of geological, genesis and structural background of gold depostis in the north Daxing'anling, Northeast China. *J. Mineral. Petrol.* **2015**, *35*, 15–24.

7. Chen, Y.J.; Zhang, C.; Wang, P.; Pirajno, F.; Li, N. The Mo deposits of Northeast China: A powerful indicator of tectonic settings and associated evolutionary trends. *Ore Geol. Rev.* **2017**, *81*, 602–640.
8. Liu, J.; Wu, G.; Qiu, H.N.; Gao, D.Z.; Yang, X.S. $^{40}Ar/^{39}Ar$ dating of gold-bearing quartz vein from the Shabaosi gold deposit at the northern end of the Great Xing'an Range and its tectonic significance. *Acta Geol. Sinica* **2013**, *87*, 1570–1579 (In Chinese).
9. Zhai, D.G.; Liu, J.J.; Ripley, E.M.; Wang, J.P. Geochronological and He–Ar–S isotopic constraints on the origin of the Sandaowanzi gold-telluride deposit, northeastern China. *Lithos* **2015**, *212–215*, 338–352.
10. Zeng, Q.D.; Liu, J.M.; Chu, S.X.; Wang, Y.B.; Sun, Y.; Duan, X.X.; Zhou, L.L.; Qu, W.J. Re–Os and U–Pb geochronology of the Duobaoshan Porphyry Cu–Mo–(Au) deposit, northeast China, and its geological significance. *J. Asian Earth Sci.* **2014**, *79*, 895–909.
11. Wang, Y.H.; Zhao, C.B.; Zhang, F.F.; Liu, J.J.; Wang, J.P.; Peng, R.M.; Liu, B. SIMS zircon U–Pb and molybdenite Re–Os geochronology, Hf isotope, and whole-rock geochemistry of the Wunugetushan porphyry Cu–Mo deposit and granitoids in NE China and their geological significance. *Gondwana Res.* **2015**, *28*, 1228–1245.
12. Li, T.; Wu, G.; Liu, J.; Hu, Y.Q.; Zhang, Y.F.; Luo, D.F.; Mao, Z.H. Fluid inclusions and isotopic characteristics of the Jiawula Pb–Zn–Ag deposit, Inner Mongolia, China. *J. Asian Earth Sci.* **2015**, *103*, 305–320.
13. Li, T.G.; Wu, G.; Liu, J.; Wang, G.R.; Hu, Y.Q.; Zhang, Y.F.; Luo, D.F.; Mao, Z.H.; Xu, B. Geochronology, fluid inclusions and isotopic characteristics of the Chaganbulagen Pb–Zn–Ag deposit, Inner Mongolia, China. *Lithos* **2016**, *261*, 340–355.
14. Shu, Q.; Lai, Y.; Sun, Y.; Wang, C.; Meng, S. Ore genesis and hydrothermal evolution of the Baiyinnuo'er zinc-lead skarn deposit, northeast China: Evidence from isotopes (S, Pb) and fluid inclusions. *Econ. Geol.* **2013**, *108*, 835–860.
15. Shu, Q.H.; Chang, Z.S.; Lai, Y.; Zhou, Y.T.; Sun, Y.; Yan, C. Regional metallogeny of Mo-bearing deposits in northeastern China, with new Re–Os dates of porphyry Mo deposits in the northern Xilamulun district. *Econ. Geol.* **2016**, *111*, 1783–1798.
16. Shu, Q.; Chang, Z.; Hammerli, J.; Lai, Y.; Huizenga, J.M. Composition and evolution of fluids forming the Baiyinnuo'er Zn–Pb skarn deposit, northeastern China: Insights from laser ablation ICP-MS study of fluid inclusions. *Econ. Geol.* **2017**, *112*, 1441–1460.
17. Liu, J.; Mao, J.W.; Wu, G.; Wang, F.; Luo, D.F.; Hu, Y.Q. Zircon U–Pb and molybdenite Re–Os dating of the Chalukou porphyry Mo deposit in the northern Great Xing'an Range, China and its geological significance. *J. Asian Earth Sci.* **2014**, *79*, 696–709.
18. Hu, X.L.; Yao, S.Z.; He, M.C.; Ding, Z.J.; Cui, Y.B.; Shen, J.; Chen, B.; Zhu, B.P. Geochemistry, U–Pb geochronology and Hf isotope studies of the Daheishan porphyry Mo deposit in Heilongjiang Province, NE China. *Resour. Geol.* **2014**, *64*, 102–116.
19. Deng, C.Z.; Sun, D.Y.; Han, J.S.; Li, G.H.; Feng, Y.Z.; Xiao, B.; Li, R.C.; Shi, H.L.; Xu, G.Z.; Yang, D.G. Ages and petrogenesis of the Late Mesozoic igneous rocks associated with the Xiaokele porphyry Cu-Mo deposit, NE China and their geodynamic implications. *Ore Geol. Rev.* **2019**, *107*, 417–433.
20. Deng, C.Z. Petrology and metallogenesis of the porphyry Cu deposits in the northern Great Xing'an Range. Ph.D. Thesis, Jilin University, Changchun, China, 2019 (in Chinese with English abstract).
21. Li, R.C.; Chen, H.Y.; Li, G.H.; Feng, Y.Z.; Xiao, B.; Han, J.S.; Deng, C.Z.; Shi, H.L. Geological characteristics and application of short wavelength infra-red technology (SWIR) in the Fukeshan porphyry copper deposit in the Great Xing'an Range area. *Earth Sci.* **2020**, *45*, 1517–1530 (In Chinese).
22. Deng, C.Z.; Sun, D.Y.; Han, J.S.; Chen, H.Y.; Li, G.H.; Xiao, B.; Li, R.C.; Feng, Y.Z.; Li, C.L.; Lu, S. Late-stage southwards subduction of the Mongol-Okhotsk oceanic slab and implications for porphyry Cu–Mo mineralization: Constraints from igneous rocks associated with the Fukeshan deposit, NE China. *Lithos* 2019, 326–327, 341–357.
23. Chen, Y.J.; Zhang, C.; Li, N.; Yang, Y.F.; Deng, K. Geology of the Mo deposits in Northeast China. *J. Jilin Univ. (Earth Sci. Ed.)* **2012**, *42*, 1223–1254 (In Chinese).
24. Wu, F.Y.; Sun, D.Y.; Ge, W.C.; Zhang, Y.B.; Grant, M.L.; Wilde, S.A.; Jahn, B.M. Geochronology of the Phanerozoic granitoids in northeastern China. *J. Asian Earth Sci.* **2011**, *41*, 1–30.
25. Sun, Y.G.; Li, B.L.; Sun, F.Y.; Ding, Q.F.; Qian, Y.; Li, L.; Xu, Q.L.; Li, Y.J. Geochronology, geochemistry, and Hf isotopic compositions of Early Permian syenogranite and diabase from the northern Great Xing'an

Range, NE China: Petrogenesis and tectonic implications. *Can. J. Earth. Sci.* **2020**, doi:10.1139/cjes-2019-0200.

26. Tang, J.; Xu, W.L.; Wang, F.; Zhao, S.; Wang, W. Early Mesozoic southward subduction history of the Mongol-Okhotsk oceanic plate: Evidence from geochronology and geochemistry of Early Mesozoic intrusive rocks in the Erguna Massif, NE China. *Gondwana Res.* **2016**, *31*, 218–240.
27. IMBGMR (Inner Mongolian Bureau of Geology and Mineral Resources). Regional Geology of Inner Mongolia. Geological Publishing House: Beijing, China, 1991; pp. 1–725 (In Chinese).
28. Miao, L.C.; Fan, W.M.; Zhang, F.Q.; Liu, D.Y.; Jian, P.; Shi, G.H.; Tao, H.; Shi, Y.R. Zircon SHRIMP geochronology of the Xinkailing-Kele complex in the northwestern Lesser Xing'an Range, and its geological implications. *Chin. Sci. Bull.* **2004**, *49*, 201–209.
29. IMBGMR (Inner Mongolian Bureau of Geology Mineral Resources). Lithostratigraphy of Inner Mongolia. China University of Geosciences Press: Wuhan, China, 1996; pp. 1–342 (In Chinese).
30. Zhang, J.H.; Ge, W.C.; Wu, F.Y.; Wilde, S.A.; Yang, J.H.; Liu, X.M. Large-scale Early Cretaceous volcanic events in the northern Great Xing'an Range, Northeastern China. *Lithos* **2008**, *102*, 138–157.
31. Gou, J.; Sun, D.Y.; Ren, Y.S.; Hou, X.G.; Yang, D.G. Geochemical and Hf isotopic compositions of Late Triassic–Early Jurassic intrusions of the Erguna Block, Northeast China: Petrogenesis and tectonic implications. *Int. Geol. Rev.* **2017**, *59*, 347–367.
32. Sun, Y.G.; Li, B.L.; Sun, F.Y.; Ding, Q.F.; Wang, B.Y.; Li, Y.J.; Wang, K. Mineralization events in the Xiaokele porphyry Cu (–Mo) deposit, NE China: Evidence from zircon U–Pb and K–feldspar Ar–Ar geochronology and petrochemistry. *Resour. Geol.* **2020**, *70*, 254–272.
33. Ge, W.C.; Wu, F.Y.; Zhou, C.Y.; Rahman, A.A. Emplacement age of the Tahe granite and its constraints on the tectonic nature of the Erguna block in the northern part of the Da Hinggan Range. *Chin. Sci. Bull.* **2005**, *50*, 2097–2105.
34. Zhou, J.B.; Wang, B.; Wilde, S.A.; Zhao, G.C.; Cao, J.L.; Zheng, C.Q.; Zeng, W.S. Geochemistry and U–Pb zircon dating of the Toudaoqiao blueschists in the Great Xing'an Range, northeast China, and tectonic implications. *J. Asian Earth Sci.* **2015**, *97*, 197–210.
35. Gustafson, L.B.; Hunt, J.P. The porphyry copper deposit at El Salvador, Chile. *Econ. Geol*. **1975**, *70*, 857–912.
36. Roedder, E. Fluid Inclusions. Rev. *Mineral. Michigan Mineral. Soc. Am.* **1984**, *12*, 644.
37. Clayton, W.M.; Mayeda, T.K. The use of bromine pent a fluoride in the extraction of oxygen from oxides and silicates for isotopic analysis. *Geochim. Cosmochim. Acta.* **1963**, *27*, 43–52.
38. Friedman, I. Deuterium content of natural waters and other substances. *Geochim. Cosmochim. Acta* **1953**, *4*, 89–103.
39. Du, A.D.; Wu, S.Q.; Sun, D.Z.; Wang, S.X.; Qu, W.J.; Markey, R.; Stain, H.; Morgan, J.; Malinovskiy, D. Preparation and certification of Re–Os dating reference materials: Molybdenite HLP and JDC. *Geost. Geoanal. Res.* **2004**, *28*, 41–52.
40. Du, A.D.; Qu, W.J.; Wang, D.H.; Li, C. Application of the Re-Os dating in economic geology. Geological Publishing House: Beijing, China, 2012; pp. 1–182 (in Chinese).
41. Ludwig, K.R. ISOPLOT 3.0: A *Geochronological Toolkit for Microsoft Excel*; Special Publication No. 4; Berkeley Geochronology Center: Berkeley, CA, USA, 2003; Volume 4, pp. 1–71.
42. Crawford, M.L. Phase equilibria in aqueous fluid inclusions. In *Fluid Inclusions: Application to Petrology*; Hollister, L.S., Crawfor, M.L., Eds; Mineralogical Association of Canada: Calgary, Canada, 1981; Volume 83, pp. 197–202.
43. Steele-MacInnis, M.; Lecumberri-Sanchez, P.; Bodnar, R.J. HOKIEFLINCS_H_2O-NACL: A Microsoft Excel spreadsheet for interpreting microthermometric data from fluid inclusions based on the PVTX properties of H_2O–NaCl. *Comput. Geosci.* **2012**, *49*, 334–337.
44. Becker, S.P.; Fall, A.; Bodnar, R.J. Synthetic fluid inclusions. XVII. PVTX properties of high salinity H_2O–NaCl solutions (N30 wt. % NaCl): Application to fluid inclusions that homogenize by halite disappearance from porphyry copper and other hydrothermal ore deposits. *Econ. Geol.* **2008**, *103*, 539–554.
45. Liu, X.; Fan, H.; Hu, F.F.; Yang, K.F.; Wen, B.J. Nature and evolution of the ore forming fluids in the giant Dexing porphyry Cu–Mo–Au deposit, southeastern China. *J. Geochem. Explor.* **2016**, *171*, 83–95.
46. Lecumberri-Sanchez, P.; Steele-MacInnis, M.; Bodnar, R.J. A numerical model to estimate trapping conditions of fluid inclusions that homogenize by halite disappearance. *Geochim. Cosmochim. Acta* **2012**, *92*, 14–22.

47. Clayton, R.N.; O'Neil, J.R.; Mayeda, T.K. Oxygen isotope exchange between quartz and water. *J. Geophys. Res. Atmos.* **1972**, *77*, 3057–3067.
48. Taylor, H.P. The application of oxygen and hydrogen isotope studies to problems of hydrothermal alteration and ore deposition. *Econ. Geol.* **1974**, *69*, 843–883.
49. Chaussidon, M.; Albarède, F.; Sheppard, S.M.F. Sulphur isotope variations in the mantle from ion microprobe analyses of micro-sulphide inclusions. *Earth Planet. Sci. Lett.* **1989**, *92*, 144–156.
50. Field, C.W.; Zhang, L.; Dilles, J.H.; Rye, R.O.; Reed, M.H. Sulfur and oxygen isotopic record in sulfate and sulfide minerals of early, deep, pre-main stage porphyry Cu–Mo and late main stage base-metal mineral deposits, Butte district, Montana. *Chem. Geol.* **2005**, *215*, 61–93.
51. Hu, X.L.; Yao, S.Z.; He, M.C.; Ding, Z.J.; Liu, M.; Cui, Y.B.; Shen, J. Sulfur and lead isotopic characteristics of Chalukou and Daheishan porphyry Mo deposits in northern segment of Da Hinggan Mountains. *Miner. Depos.* **2014**, *33*, 776–784 (In Chinese).
52. Liu, J.;Mao, J.W.; Wu, G.; Wang, F.; Luo, D.F.; Hu, Y.Q. Fluid inclusions and H–O–S–Pb isotope systematics of the Chalukou giant porphyry Mo deposit, Heilongjiang Province, China. *Ore Geol. Rev.* **2014**, *59*, 83–96.
53. Zhang, F.F.; Wang, Y.H.; Liu, J.J.; Wang, J.P.; Zhao, C.B.; Song, Z.W. Origin of the Wunugetushan porphyry Cu–Mo deposit, Inner Mongolia, NE China: Constraints from geology, geochronology, geochemistry, and isotopic compositions. *J. Asian Earth Sci.* **2016**, *117*, 208–224.
54. Mi, K.F.; Liu, Z.J.; Li, C.F.; Liu, R.B.; Wang, J.P.; Peng, R.M. Origin of the Badaguan porphyry Cu-Mo deposit, Inner Mongolia, northeast China: Constraints from geology, isotope geochemistry and geochronology. *Ore Geol. Rev.* **2017**, *81*, 154–172.
55. Zartman, R.; Doe, B. Plumbotectonics: The model. *Tectonophysics* **1981**, *75*, 135–162.
56. Guo, X.G.; Li, J.W.; Zhang, D.H.; Xue, F.; Xian, H.B.; Wang, S.J.; Jiao, T.L. Petrogenesis and tectonic setting of igneous rocks from the Dongbulage porphyry Mo deposit, Great Hinggan Range, NE China: Constraints from geology, geochronology, and isotope geochemistry. *Ore Geol. Rev.* **2020**, *120*, 103326.
57. Guo, F.; Fan, W.M.; Gao, X.F.; Li, C.W.; Miao, L.C.; Zhao, L.; Li, H.X. Sr–Nd–Pb isotope mapping of Mesozoic igneous rocks in NE China: Constraints on tectonic framework and Phanerozoic crustal growth. *Lithos* **2010**, *120*, 563–578.
58. Ohmoto, H.; Rye, R.O. Isotopes of sulfur and carbon. In *Geochemistry of Hydrothermal Ore Deposits;* Barnes, H.L., Ed.; Wiley: New York, NY, USA, 1979; pp. 509–567.
59. Cooke, D.R.; Hollings, P.; Wilkinson, J.J.; Tosdal, R.M. Geochemistry of porphyry deposits. In *Treatise on Geochemistry*, 2nd ed; Holland, H.D., Turekian, K.K., Eds.; Elsevier: Oxford, UK, 2014; pp. 357–381.
60. Roedder, E.; Bodnar, R.J. Geologic pressure determinations from fluid inclusion studies. *Annu. Rev. Earth Planet. Sci.* **1980**, *8*, 263–301.
61. Driesner, T.; Heinrich, C.A. The system H_2O–NaCl. Part I: Correlation formulae for phase relations in temperature–pressure-composition space from 0 to 1000 °C, 0 to 5000 bar, and 0 to 1 XNaCl. *Geochim. Cosmochim. Acta* **2007**, *71*, 4880–4901.
62. Rusk, B.G.; Reed, M.; Dilles, J.H. Fluid inclusion evidence for magmatic-hydrothermal fluid evolution in the porphyry coppermolybdenum deposit at Butte, Montana. *Econ. Geol.* **2008**, *103*, 307–332.
63. Pirajno, F. Hydrothermal Processes and Mineral Systems. Springer Science & Business Media: Berlin, Germany, 2009; p. 1250.
64. Barnes, H.L. Solubilities of ore minerals. In *Geochemistry of Hydrothermal Ore Deposits;* Barnes, H.L., Ed.; Wiley: New York, NY, USA, 1979; pp. 404–460.
65. Rust, A.C.; Cashman, K.V.; Wallace, P.J. Magma degassing buffered by vapor flow through brecciated conduit margins. *Geology* **2004**, *32*, 349–352.
66. Harris, A.C.; Golding, S.D.; White, N.C. Bajo de la Alumbrera copper–gold deposit: Stable isotope evidence for a porphyry-related hydrothermal system dominated by magmatic aqueous fluids. *Econ. Geol.* **2005**, *100*, 863–886.
67. Lang, X.H.; Deng, Y.L.; Wang, X.H.; Tang, J.X.; Xie, F.W.; Yang, Z.Y.; Yin, Q.; Jiang, K. Reduced fluids in porphyry copper-gold systems reflect the occurrence of the wall-rock thermogenic process: An example from the No.1 deposit in the Xiongcun district, Tibet, China. *Ore Geol. Rev.* **2020**, *118*, 103212.
68. Rye, R.O.; Ohmoto, H. Sulfur and carbon isotopes and ore genesis: A review. *Econ. Geol.* **1974**, *69*, 826–842.

69. Hedenquist, J.W.; Arribas, A.; Reynolds, T.J. Evolution of an intrusion- centered hydrothermal system: Far southeast-lepanto porphyry and epithermal Cu–Au deposits, Philippines. *Econ. Geol.* **1998**, *93*, 373–404.
70. Koděra, P.; Lexa, J.; Rankin, A.H.; Fallick, A.E. Epithermal gold veins in a caldera setting: Banská Hodruša, Slovakia. *Mineral. Depos.* **2005**, *39*, 921–943.
71. Zhai, D.G.; Liu, J.J.; Tombros, S.; Williams-Jones, A.E. The genesis of the Hashitu porphyry molybdenum deposit, Inner Mongolia, NE China: Constraints from mineralogical, fluid inclusion, and multiple isotope (H, O, S, Mo, Pb) studies. *Miner. Dep.* **2018**, *53*, 377–397.
72. Zhang, F.F.; Wang, Y.H.; Liu, J.J.; Wang, J.C. Ore genesis and hydrothermal evolution of the Wulandele Mo deposit, Inner Mongolia, Northeast China: Evidence from geology, fluid inclusions and H–O–S–Pb isotopes. *Ore Geol. Rev.* **2018**, *93*, 181–199.
73. Audétat, A.; Pettke, T.; Heinrich, C.A.; Bodnar, R.J. The composition of magmatic–hydrothermal fluids in barren and mineralized intrusions. *Econ. Geol.* **2008**, *103*, 877–908.
74. Sun, W.D.; Huang, R.F.; Li, H.; Hu, Y.B.; Zhang, C.C.; Sun, S.J.; Zhang, L.P.; Ding, X.; Li, C.Y.; Zartman, R.E.; et al. Porphyry deposits and oxidized magmas. *Ore Geol. Rev.* **2015**, *65*, 97–131.
75. Cooke, D.R.; Hollings, P.; Walshe, J.L. Giant porphyry deposits: Characteristics, distribution, and tectonic controls. *Econ. Geol.* **2005**, *100*, 801–818.
76. Sun, H.R.; Huang, Z.L.; Li, W.B.; Ye, L.; Zhou, J.X. Geochronological, isotopic and mineral geochemical constraints on the genesis of the Diyanqinamu Mo deposit, Inner Mongolia, China. *Ore Geol. Rev.* **2015**, *65*, 70–83.
77. Mungall, J.E. Roasting the mantle: Slab melting and the genesis of major Au and Au-rich Cu deposits. *Geology* **2002**, *30*, 915–918.
78. Roedder, E. Fluid inclusion studies on the porphyry-type ore deposits at Bingham, Utah, Butte, Montana, and Climax, Colorado. *Econ. Geol.* **1971**, *66*, 98–118.
79. Holland, H.D. Granites, solutions, and basemetal deposits. *Econ. Geol.* **1972**, *67*, 281–301.
80. Crerar, D.A.; Barnes, H. Ore solution chemistry; V, solubilities of chalcopyrite and chalcocite assemblages in hydrothermal solution at 200 to 350 °C. *Econ. Geol.* **1976**, *71*, 772–794.
81. Henley, R.; McNabb, A. Magmatic vapor plumes and ground-water interaction in porphyry copper emplacement. *Econ. Geol.* **1978**, *73*, 1–20.
82. Williams-Jones, A.E.; Heinrich, C.A. 100th Anniversary special paper: Vapor transport of metals and the formation of magmatic–hydrothermal ore deposits. *Econ. Geol.* **2005**, *100*, 1287–1312.
83. Seo, J.H.; Guillong, M.; Heinrich, C.A. The role of sulfur in the formation of magmatic–hydrothermal copper–gold deposits. *Earth Planet. Sci. Lett.* **2009**, *282*, 323–328.
84. Chen, Y.J.; Pirajno, F.; Li, N.; Guo, D.S.; Lai, Y. Isotope systematic and fluid inclusion studies of the Qiyugou breccias pipe-hosted gold deposit, Qinling Orogen, Henan Province, China: Implications for ore genesis. *Ore Geol. Rev.* **2009**, *35*, 245–261.
85. Li, N.; Ulrich, T.; Chen, Y.-J.; Thomsen, T.B.; Pease, V.; Pirajno, F. Fluid evolution of the Yuchiling porphyry Mo deposit, East Qinling, China. *Ore Geol. Rev.* **2012**, *48*, 442–459.
86. Yang, Y.F.; Li, N.; Chen, Y.J. Fluid inclusion study of the Nannihu giant porphyry Mo–W deposit, Henan Province, China: Implications for the nature of porphyry ore-fluid systems formed in a continental collision setting. *Ore Geol. Rev.* **2012**, *46*, 83–94.
87. Ulrich, T.; Guenther, D.; Heinrich, C.A. Gold concentrations of magmatic brines and the metal budget of porphyry copper deposits. *Nature* **1999**, *399*, 676–679.
88. Heinrich, C.A. The physical and chemical evolution of low-salinity magmatic fluids at the porphyry to epithermal transition: A thermodynamic study. *Miner. Deposita* **2005**, *39*, 864–889.
89. Liang, H.Y.; Sun, W.D.; Su, W.C.; Zartman, R.E. Porphyry copper-gold mineralization at Yulong, China, promoted by decreasing redox potential during magnetite alteration. *Econ. Geol.* **2009**, *104*, 587–596.
90. Hemley, J.J.; Cygan, G.L.; Fein, J.B.; Robinson, G.R.; Dangelo, W.M. Hydrothermal ore-forming processes in the light of studies in rock-buffered systems. I. Iron-copperzinc-lead sulfide solubility relations. *Econ. Geol. Bull. Soc. Econ. Geol.* **1992**, *87*, 1–22.
91. Liu, W.; Mcphail, D. Thermodynamic properties of copper chloride complexes and copper transport in magmatic-hydrothermal solutions. *Chem. Geol.* **2005**, *221*, 21–39.

92. Landtwing, M.R.; Pettke, T.; Halter, W.E.; Heinrich, C.A.; Redmond, P.B.; Einaudi, M.T.; Kunze, K. Copper deposition during quartz dissolution by cooling magmatic–hydrothermal fluids: The Bingham porphyry. *Earth Planet. Sci. Lett.* **2005**, *235*, 229–243.
93. Hezarkhani, A.; William-Jones, A.E.; Gammons, C.H. Factors controlling copper solubility and chalcopyrite deposition in the Sungun porphyry copper deposit, Iran. *Miner. Dep.* **1999**, *34*, 770–783.
94. Fournier, R.O. Hydrothermal process related to movement of fluid from plastic into brittle rock in the magmatic-epithermal environment. *Econ. Geol.* **1999**, *94*, 1193–1211.
95. Sillitoe, R.H. Porphyry copper systems. *Econ. Geol.* **2010**, *105*, 3–41.
96. Simon, A.C.; Ripley, E.M. The role of magmatic sulfur in the formation of ore deposits. *Rev. Mineral. Geochem.* **2011**, *73*, 513–578.
97. Henley, R.W.; King, P.L.; Wykes, J.L.; Renggli, C.J.; Brink, F.J.; Clark, D.A.; Troitzsch, U. Porphyry copper deposit formation by sub-volcanic sulphur dioxide flux and chemisorption. *Nat. Geosci.* **2015**, *8*, 210–215.
98. Fontboté, L.; Kouzmanov, K.; Chiaradia, M.; Pokrovski, G.S. Sulfide minerals in hydrothermal deposits. *Elements* **2017**, *13*, 97–103.
99. Watanabe, Y.; Sato, R.; Sulaksono, A. Role of potassic alteration for porphyry cu mineralization: Implication for the absence of porphyry cu deposits in japan. *Resour. Geol.* **2018**, *68*, 195–207.
100. Zhu, X.P.; Duo, J.; Li, G.M.; Liu, H.F.; Chen, H.A.; Ma, D.F.; Liu, C.Q.; Wei, L.J. High-oxidation-governed fluid evolution in the Naruo porphyry Cu–Au deposit, Tibet, China. *Ore Geol. Rev.* **2020**, *117*, 103318.
101. Taylor, H.P. Oxygen and hydrogen isotope relationships in hydrothermal mineral deposits. *Geochem. Hydrothermal Ore Depos.* **1997**, *3*, 229–302.
102. Simmons, S.F.; White, N.C.; John, D.A. Geological Characteristics of Epithermal Precious and Base Metal Deposits. *Econ. Geol.* **2005**, *100*, 485–522.

© 2020 by the authors. Licensee MDPI, Basel, Switzerland. This article is an open access article distributed under the terms and conditions of the Creative Commons Attribution (CC BY) license (http://creativecommons.org/licenses/by/4.0/).